Ore Geology Reviews 140 (2022) 104572

Contents lists available at ScienceDirect

Ore Geology Reviews

journal homepage: www.elsevier.com/locate/oregeorev

Unveiling the polyphasic evolution of the Neoarchean IOCG Salobo deposit, Carajás Mineral Province, Brazil: Insights from magnetite trace elements and sulfur isotopes

Yuri Tatiana Campo-Rodríguez [a,*], María Emilia Schutesky [a], Claudinei Gouveia de Oliveira [a], Martin John Whitehouse [b]

[a] Instituto de Geociências, Universidade de Brasília, Brasília, DF 70910-900, Brazil
[b] Swedish Museum of Natural History – Nordsims, Stockholm, Sweden

ARTICLE INFO

Keywords:
Iron-oxide copper-gold deposits
Carajás Mineral Province
Sulfur isotopes
Magnetite geochemistry

ABSTRACT

The Salobo iron oxide copper-gold (IOCG) deposit host an important Cu-mineralization of the Carajás Mineral Province. The ore is characterized by an association of (bornite-chalcocite-digenite) hosted by magnetite and biotite-garnet schists. These rocks record distinct stages of superimposed hydrothermal alteration and dynamic metamorphism. Three different occurrences of magnetite constitute the magnetite bodies: a pristine to inclusion-poor Mgt I; inclusion-rich magnetite-bearing breccia Mgt II, and the granoblastic-foliated Mgt III. In general, the magnetite types present a similar trace element composition with some variations in Si, Al, Mg and K indicating that the magnetite types share the same magmatic-hydrothermal origin with post-formation processes (dissolution/reprecipitation) recorded in Mgt III. In addition, sulfur isotope signatures for chalcopyrite (1.3–3.35‰), pyrrhotite (0.88–1.98‰), and pyrite (1.7–5.04‰) associated with magnetite I and II, are consistent with a magmatic-hydrothermal sulfur source at Salobo without/or minimal external sulfur contributions. Our data indicate that ore-forming fluids for Salobo ore could have undergone sulfur disproportionation processes during sulfide formation due to magnetite precipitation, which results in the classic IOCG mineral association of chalcopyrite + magnetite described for the first time in this contribution. Therefore, the main mineralization event in the Salobo deposit could be coeval with similar IOCG deposits in the Carajás Mineral Province related to the Neoarchean magmatism at ca. 2.7 Ga. Subsequent deformation and low-grade dynamic metamorphism related to reactivation of the Cinzento Shear Zone (ca. 2.5 Ga) and A-type granite emplacement probably Paleoproterozoic in age resulted in remobilization-recrystallization of magnetite and Cu-sulfides.

1. Introduction

The Carajás Mineral Province is characterized by a complex geological-metallogenic evolution from the Archean to Paleoproterozoic, which involves several mineralizing events within distinct geotectonic environments (Grainger et al., 2008; Tavares et al., 2018). Along the regional-scale WNW-ESE-trending Cinzento shear zone occurs the Salobo deposit (Moreto et al., 2015; de Melo et al., 2019), which displays an intense deformation and pervasive hydrothermal alteration in the host rock of the deposit (Moreto et al., 2015).

Contrarily to the most common type of IOCG deposits in Carajás (i.e., chalcopyrite-bearing), the Salobo ore consists of a bornite-chalcocite-digenite assemblage hosted by garnet-biotite and magnetite schists. The available genetic models linked the mineralization with the Cinzento shear-zone reactivation, due to intense dynamic recrystallization and hydrothermal alteration overprint (deMelo et al., 2017), as well as late remobilization stages in a polycyclic evolution of this lineament (Tassinari et al., 2003). However, a detailed characterization of the influence of multiple syn and post-kynematic recrystallization in the Salobo ore evolution has not been addressed so far.

Trace element geochemistry of magnetite has been used as a fingerprint for mineral exploration based on discriminant diagrams that differentiate various mineralization styles since it reflects both the formation conditions and the composition of magma or hydrothermal

* Corresponding author.
E-mail addresses: ytcampor@unal.edu.co (Y.T. Campo-Rodríguez), maria_emilia@unb.br (M.E. Schutesky), gouveia@unb.br (C.G. de Oliveira), martin.whitehouse@nrm.se (M.J. Whitehouse).

https://doi.org/10.1016/j.oregeorev.2021.104572
Received 6 March 2021; Received in revised form 20 October 2021; Accepted 5 November 2021
Available online 12 November 2021

solutions from which crystallizes, (Dupuis and Beaudoin, 2011; Dare et al., 2014; Nadoll et al., 2014; Wen et al., 2017). Moreover, magnetite textures record processes of recrystallization, dissolution, and reprecipitation (Hu et al., 2014; Hu et al., 2015; Wen et al., 2017; Deditius et al., 2018; Rojas et al., 2018; Huang and Beaudoin, 2019), whereas sulfur isotopic signature delineates the sulfur source and offers insights into the fluid-rock interaction providing the geodynamic environment in which the mineralizing process occurs (LaFlamme et al., 2016). Conceptual

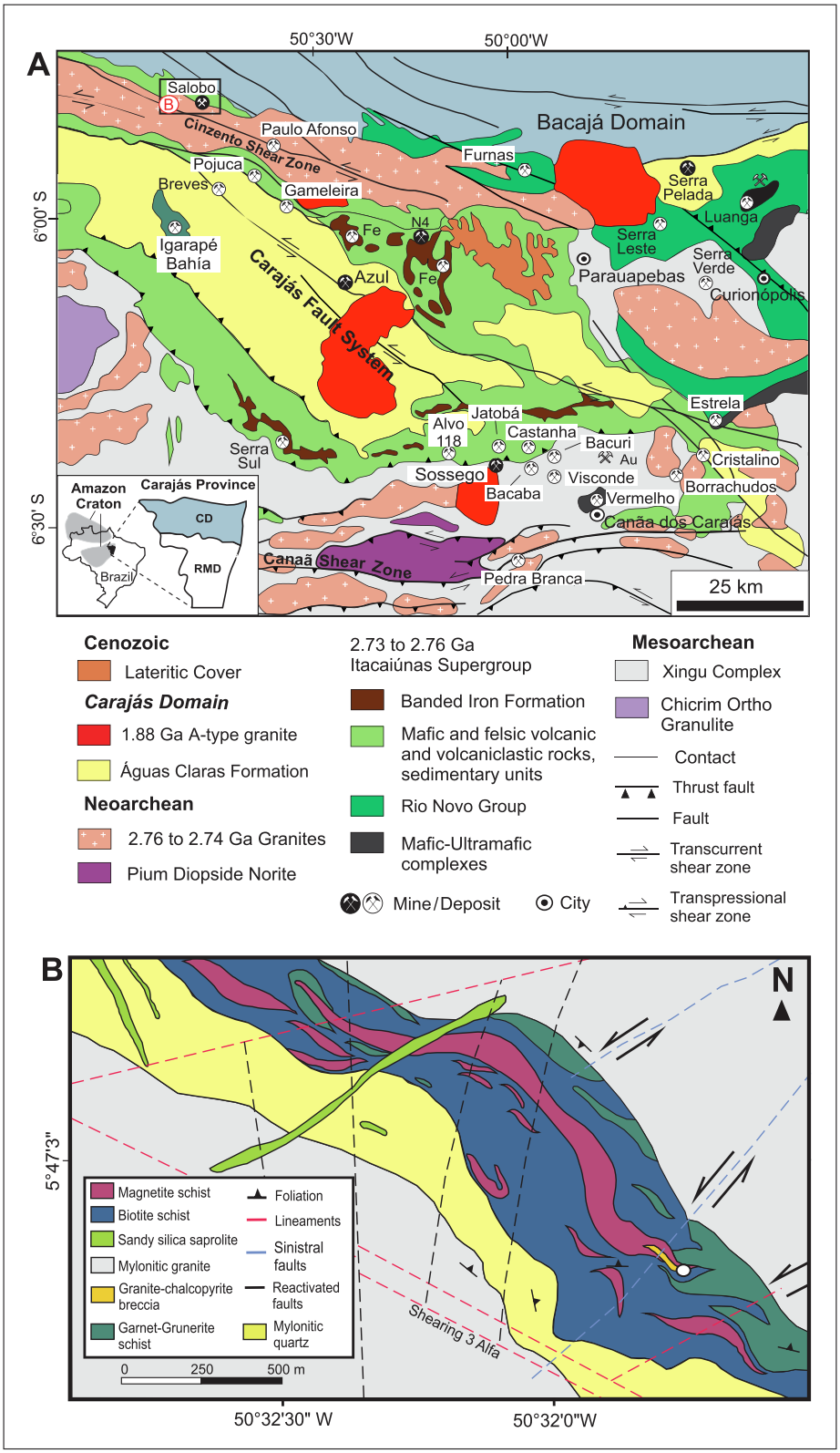

Fig. 1. (A) Geological map of the Carajás Domain with the locations of the main mines and ore deposits, including the Salobo deposit (Black rectangle) (Modified from Vasquez et al., 2008; de Melo et al., 2019). Abbreviations: CD = Carajás Domain, RMD = Rio Maria Domain. (B) Simplified geological map of the Salobo mine, depicting the host rocks and approximate sample location (*white circle*).

models on IOCG formation that involve a magmatic sulfur source (Acosta-Góngora et al., 2014; Pollard, 2006; Schlegel et al., 2017) have suggested that an oxidized sulfur source is needed to generate the paragenetic association between iron oxides and Cu-sulfides (Barton, 2014; Hitzman et al., 1992; Richards and Mumin, 2013; Williams et al., 2005). Hence, the reduction of sulfur is critical for the Cu-sulfide ore precipitation (Barton, 2014; Williams et al., 2005). Consequently, the use of trace element geochemistry combined with sulfur isotope is useful to unveil the early processes that result in the formation of the ore.

This paper presents the results of petrography and mineral chemistry (electron microprobe analysis – EMPA) of magnetite, and isotopic studies (chalcopyrite, pyrite, and pyrrhotite SIMS sulfur) from the ore paragenesis (magnetite + chalcopyrite) of the Salobo IOCG deposit. This information allows us to constrain the conditions of sulfide and ore deposition at the Salobo deposit, from early magmatic-hydrothermal stages to late thermal overprint, which produce ore remobilization and dynamic recrystallization. In this context, the Salobo deposit would represent an exceptional case of metamorphosed Neoarchean IOCG deposit with hydrothermal alteration and ore zoning still partially preserved.

2. Geological context

2.1. The Carajás Mineral Province

The Carajás Mineral Province (CMP) constitutes an Archean crustal segment located in the southeastern of the Amazonian Craton in northern Brazil (DOCEGEO, 1988; Vasquez et al., 2008). The CMP includes two major tectonic domains: the Mesoarchean Rio Maria Domain in the south and the Neoarchean Carajás Domain (CD) in the north, limited by the regional E-W Cinzento shear-zone (Fig. 1A; Vasquez et al., 2008).

The oldest rocks of the Carajás Domain are granulites of the Chicrim-Cateté Orthogranulite (3002 ± 14 Ma, U-Pb zircon; Pidgeon et al., 2000) and gneisses and migmatite of the Xingu Complex (2974 ± 15 Ma, Pb-Pb evaporation zircon age, Avelar et al., 1999; 3066 ± 6,6 Ma, U-Pb zircon, Delinardo da Silva, 2014). The basement is also composed of the Mesoarchean Canaã dos Carajás Granite (ca. 2.96–2.93 Ga; Feio et al., 2013). These rocks have experimented several reactivation events during the Archean and Paleoproterozoic (2860 ± 2 Ma, U-Pb zircon, Machado et al., 1991; 2859 ± 9 Ma, U-Pb zircon, Pidgeon et al., 2000; ca. 2.76–2.73 Ga, DOCEGEO, 1988; Machado et al., 1991; 2573 ± 3 Ma; Machado et al., 1991; ca. 1.88 Ga, Machado et al., 1991).

Metavolcano-sedimentary rocks of the Itacaiúnas Supergroup rest unconformably on the basement rocks (DOCEGEO, 1988; Machado et al., 1991; Pinheiro and Holdsworth, 2000; Pollard et al., 2018). This is subdivided into metavolcano-sedimentary sequences, namely the Igarapé Salobo, Igarapé Pojuca, Grão Pará and Igarapé Bahia groups, all formed between 2.76 and 2.73 Ga (DOCEGEO, 1988; Machado et al., 1991). The latter include the jaspilites of the Carajás Formation, which host the iron deposits of Carajás (Silva et al., 2013; Justo et al., 2020).

Mafic-ultramafic intrusions (DOCEGEO, 1988; Machado et al., 1991; Feio et al., 2013) with moderate spilitization and sub-greenschist metamorphism (Martins et al., 2017) are represented by the Serra Leste (Machado et al., 1991; Ferreira Filho et al., 2007; Mansur et al., 2020) and the Carajás suites. The former host sulfide-rich Cr-PGE mineralization in the Luanga Complex (Mansur et al., 2020), whereas in the later, world-class lateritic Ni deposits form, such as the Serra da Onça, Serra do Puma, and Vermelho (Siepierski and Ferreira Filho, 2016). Moreover, these complexes constitute a major magmatic event coeval with the extensive basaltic volcanism of the Grão Pará Group (Machado et al., 1991; Ferreira Filho et al., 2007).

Main regional episodes of granitic plutonism recorded in the Carajás Domain includes the Neoarchean ca. 2.76 to 2.73 Ga A-type sub-alkaline granites (e.g., Planalto, Plaquê, Estrela Complex, Serra do Rabo and Igarapé Gelado; Feio et al., 2013; Moreto et al., 2015). Additionally, the peralkaline to meta-aluminous granites of Old Salobo (2573 ± 3 Ma; Machado et al., 1991) and Itacaiúnas granites (2560 ± 37 Ma; Souza et al., 1996) were identified locally within the Cinzento shear zone (deMelo et al., 2017). Finally, Paleoproterozoic ca. 1.88 Ga anorogenic granitic plutons comprise the alkaline and sub-alkaline Serra dos Carajás, Young Salobo, Pojuca, and Cigano (Machado et al., 1991; Dall'Agnol et al., 2006), which are observed throughout all of the Amazon Craton.

Orosirian-Siderian sedimentary rocks of the Águas Claras Formation unconformably covers the Itacaiúnas Supergroup. It is composed of sandstones and siltstones deposited in fluvial to shallow marine environment (Nogueira et al., 1995; Tavares et al., 2018; Araújo Filho et al., 2020).

2.2. Deformation and metamorphism in the Carajás Mineral Province

The Carajás Mineral Province is characterized by a structural configuration of E-W oriented rocks surrounded by the prominent fault systems of the Carajás and Cinzento shear zones (Fig. 1A) (de Freitas Toledo et al., 2018 and references therein), thought to be formed within an oblique setting with subsequent stages of transpression and transtension (Machado et al., 1991; Pinheiro and Holdsworth, 2000; Souza and Vieira, 2000). These structures entail a complex tectonic evolution characterized by several structural reactivation events that lasted for hundreds of millions of years from 2.87 to 2.83 Ga to 1.88 Ga (Tavares et al., 2018).

The first deformation/metamorphism event forms a pull-apart Carajás Basin at ca 2.76–2.70 Ga (Machado et al., 1991; Pinheiro and Holdsworth, 2000; Tavares et al., 2018), and steeply dipping linear shear zones with 2.76–2.73 Ga syn-tectonic intrusions and Neoarchean IOCG mineralizations (da Costa et al., 2020). Accordingly, this event is coeval to the emplacement of granitic plutons (Tavares et al., 2018) and the high-grade regional metamorphism (Machado et al., 1991). Otherwise, DOCEGEO (1988) and Martins et al. (2017) link the deposition of the Carajás Basin with a continental rift opening.

Subsequent events consist of basin inversion and weak intracontinental orogeny (2.68–2.63 Ga), followed by a Rhyacian collision between the Carajás and Bacajá blocks during the Transamazonian cycle (2.1–2.05 Ga) that reflects metamorphism by tectono-thermal reworking (Tavares et al., 2018). The Utamã magmatism marks the last major deformation event that caused crustal thickening and regional metamorphism, which is related to extensional/transtensional reactivation in a shallow, brittle environment (Machado et al., 1991; Pinheiro and Holdsworth, 2000; Tavares et al., 2018), ending with late post-orogenic sedimentation and 1.88 Ga anorogenic alkaline A-type magmatism. For a recent review on the structural evolution of the Carajás Mineral Province, the reader is referred to the work of Tavares et al., (2018).

2.3. The Salobo deposit

Salobo is the largest copper deposit in Brazil, with resources of 1,112 Mt Cu-Au at 0.69% Cu and 0.43 g/t Au (VALE, 2012 - *internal report*). It is located in the Cinzento Shear Zone near the northern limit of the Carajás Domain (CD; Fig. 1A, B) and it is characterized by intense deformation and widespread mylonitic foliation, which is defined by quartz and mafic minerals. The hydrothermal alteration form preserved subvertical lens-shaped magnetite-rich and copper orebodies that occur mainly at the central zone of the deposit within hydrothermally altered granitic rocks and garnet-biotite schists (Valadão, 2019). These rocks dip in high-angle structurally controlled by the regional ductile-brittle Cinzento shear zone (de Melo et al., 2019).

The proximity of the deposit with the Cinzento strike-slip lineament entails intense deformation and pervasive hydrothermal alteration. The intense mylonitic foliation of the deposit rocks wipes out the deposit host rocks' original features (deMelo et al., 2017). Due to the poor preservation of the primary mineralogy and textures, the geology and

the metallogenetic evolution of the Salobo deposit have been a matter of debate in the literature (Lindenmayer, 1990; Huhn Bacelar, 1996; Lindenmayer and Teixeira, 1999; Requia et al., 2003; Tassinari et al., 2003; deMelo et al., 2017; Tavares et al., 2018; de Melo et al., 2019; Valadão, 2019).

At first, the Salobo deposit was interpreted as a VMS type with the quartzites, gneisses, amphibolites, and iron formations of the Salobo Group as the host rocks (Lindenmayer, 1990). Lindenmayer (1990) interpreted high-grade metamorphism with pyroxene hornfels facies (Table 1) and two hydrothermal alteration events coherent with amphibolite and greenschist facies around 2.5 Ga (Table 1), both related to shearing stress conditions.

Afterwards, Huhn Bacelar (1996) included the Salobo mineralization in the IOCG deposit class (Cu-Au-U-ETR) due to the signs of albitization processes followed by potassic-propylitic alteration in the deposit, the high salinity (20%NaCl) and temperature (>350 °C) fluids, besides, the lack of pyrite in the ore assemblage (magnetite-bornite-chalcocite). Requia and Fontboté (1999) observed that most iron oxides that composed the iron formations were, in fact, of epigenetic origin and associated with a hydrothermal system that resulted from intense alkalic-Fe metasomatism (Requia and Fontboté, 2000).

Tassinari et al. (2003) suggested three stages for the deposit evolution based on Pb-Pb age in chalcocite (2705 ± 42 Ma), tourmaline (2587 ± 150 Ma), chalcopyrite (2427 ± 130 Ma), and magnetite (2112 ± 12 Ma): (i) syngenetic development of the copper mineralization, during the volcanism and deposition of the Salobo, Pojuca, and Grão Pará Groups at ca. 2.7 Ga, (ii) reprecipitation (epigenetic mineralization) caused by the tectonic reactivation episodes related to the Cinzento shear zone evolution and the intrusion of the Old Salobo Granite at ca. 2.5 Ga, and (iii) hydrothermal alteration associated with late-stage retrograde metamorphism of greenschist facies at ca. 2.1 Ga.

Conversely, Requia et al. (2003) proposed that the deposit formation resulted from the intrusion of the alkaline, metaluminous Old Salobo Granite, based on a molybdenite Re-Os age of 2576 ± 8 and 2562 ± 8 Ma. Following this rationale, deMelo et al. (2017) reinforced that the main IOCG mineralization event probably occurred simultaneously as the intrusion of the Old Salobo Granite at ca. 2.5 Ga. deMelo et al. (2017) related the ore genesis to dynamic metamorphism, metasomatism, and mineralization, and proposed a paragenetic sequence evolving from sodic-calcic alteration (hastingsite-actinolite) to iron enrichment and tourmaline formation (grunerite-almandine-fayalite and tourmaline). Late-Archean reactivation of Cinzento Shear zone caused ore remobilization forming magnetite and ore cogenetic with biotite (potassic alteration); and post-ore hydrothermal alteration (propylitic alteration and hematite formation). deMelo et al. (2017) also considered protoliths to be part of the Xingu Complex (ca. 2.9 Ma) and the Igarapé Gelado (2763 ± 4.4 Ma; deMelo et al., 2017). Finally, de Melo et al. (2019) added a magmatic sulfur source for the high-temperature hydrothermal system reaching 565° ± 50 °C (quartz-biotite pairs).

2.4. A new view of the Salobo deposit

Valadão (2019) recently showed some inconsistencies in the paragenetic sequences regarding the relationship between the gangue-ore assemblage. In particular, the low-temperature association (digenite-chalcocite) was proposed due to the bornite-solid solution reaction, expressed in fine symplectic intergrowth in a Cu-Fe-S system. Thus, the digenite-chalcocite assemblage, previously considered paragenetic with high-temperature minerals (fayalite-ferrosilite) in the same mineralization event, could result from later alteration stages. Thus, the genesis

Table 1
Summary of alteration stages and mineral association data for the Salobo IOCG deposit.

Rocks	Related Age	Causes hydrothermal alteration	Mineral assemblage	Temperature	Isotope Signature	References
Hydrothermal altered granites, iron formation, quartzites and metagraywackes	2758 ± 2 Ma (U-Pb zrn; Machado et al., 1991)	Metamorphism (Facies pyroxene-hornfels)	Fayalite-garnet-hastingsite-magnetite	~750 °C	No data	(Lindenmayer, 1990; Lindenmayer and Teixeira, 1999)
	Interval of 2581–2551 Ma (U-Pb mnz; Machado et al., 1991)	Hydrothermal alteration I (hydration - facies amphibolite)	Grunerite - biotite – almandine – magnetite. (Pseudomorphic substitution of previously mineral assemblage)	~650–550 °C		
		Hydrothermal alteration II (facies greenschist)	Chloritization of Fe-Mg minerals. Greenalite-chlorite	~370 °C		
Garnet-biotite and Magnetite schists	2551 ± 2 Ma (U-Pb mnz Machado et al., 1991) 2576 ± 1.4 Ma (Re-Os mol; Requia et al., 2003) 2535 ± 8.4 Ma (U-Pb zrn; deMelo et al., 2017)	Metamorphism -ductile deformation K- biotite-garnet-quartz	Biotite-almandine-titanite-quartz-k feldspar- magnetite	650–550 °C (Souza and Vieira, 2000) 565 ± 50 °C (de Melo et al., 2019)	$\delta^{34}S$: 0.2–1.6‰ (Ccp; Requia and Fontboté, 2000) $\delta^{34}S$: −0.27 to −0.30‰ $\Delta^{33}S$: −0.15‰ to −0.30‰ (ccp; Bühn et al., 2012)	(deMelo et al., 2017; de Melo et al., 2019)
Magnetite schist	Paleo-proterozoic 2.1–1.88 Ga (Re-Os mol; Requia et al., 2003)	Ca-bearing fluids and chloritization – A-type granitic magmatism Hydrolytic-prophylitic alteration	Chlorite-epidote-greenalite-pyrosmalite Bornite-chalcocite-digenite-calcite-fluorite	~360° C (Requia and Fontboté, 2000) <370 °C (Souza and Vieira, 2000) 269–305 °C (Bernard Prado et al., 2019) <335 °C (de Melo et al., 2019)	$\delta^{34}S$: 0.2–1.6‰ (bn; Requia and Fontboté, 2000) $\delta^{34}S$: 0.81 to 1.28‰ (ccp n = 3) $\delta^{34}S$: −0.37 to + 1.63‰ (bn; de Melo et al., 2019) $\delta^{34}S$: −0.49 to −0.26‰ $\Delta^{33}S$: −0.14‰ to −0.05‰ (ccp; Santiago et al., 2021)	

Note: Mineral abbreviations = Bn: bornite, Ccp: chalcopyrite, Mnz: monazite, Mol: molybdenite, Zrn: zircon.

and evolution of the Salobo deposit is very complex and characterized by superimposed deformational and hydrothermal events. Accordingly, the hydrothermal alteration at the Salobo deposit is characterized by different styles, types, and distribution of mineral associations. The paragenetic evolution at Salobo, following Valadão (2019), is shown in Fig. 2. Hydrothermal assemblages evolved from early sodic alteration accompanied by Ca-Fe alteration (iron enrichment) to potassic alteration with biotite. The copper-gold mineralization is spatially associated with the iron enrichment and potassic alteration zones. The late hydrothermal stage is defined by chlorite alteration, low-temperature Cu-sulfide assemblage (bornite-chalcocite-covellite) accompanied by Fe-rich hydrolytic alteration (pyrosmalite-greenalite-hematite).

The occurrence of scapolite-tourmaline evidence an incipient sodic alteration. Marialitic scapolite occurs as a selective replacement of plagioclase. The Ca-Fe enrichment consists of fayalite-ferrosilite-grunerite-hornblende partially preserved within the schists. Grunerite occurs as subidioblastic crystals near to grunerite, commonly occurring as idioblastic porphyroblasts parallel to the mylonitic foliation. Ferrosilite is presented as granular crystals disseminated in the magnetite-breccia domain (chalcopyrite breccia). Magnetite displays granular to massive habit. Accessory minerals consist of allanite, apatite, and uraninite.

The Cu-Au ore assemblage occurs in dipping lenses or elongated bodies along the mylonitic foliation associated with chalcopyrite breccia. The highest content of Cu-Fe-sulfides is characteristic of the Cu-mineralization stage. It is composed of chalcopyrite, actinolite, and subordinated pyrrhotite, pyrite, pentlandite, and siegenite. Pyrrhotite occurs as exsolution lamellae in pyrite, which in turn is texturally associated with pentlandite in some places. Actinolite commonly occurs filling fractures and enveloping coarse grains of primary magnetite.

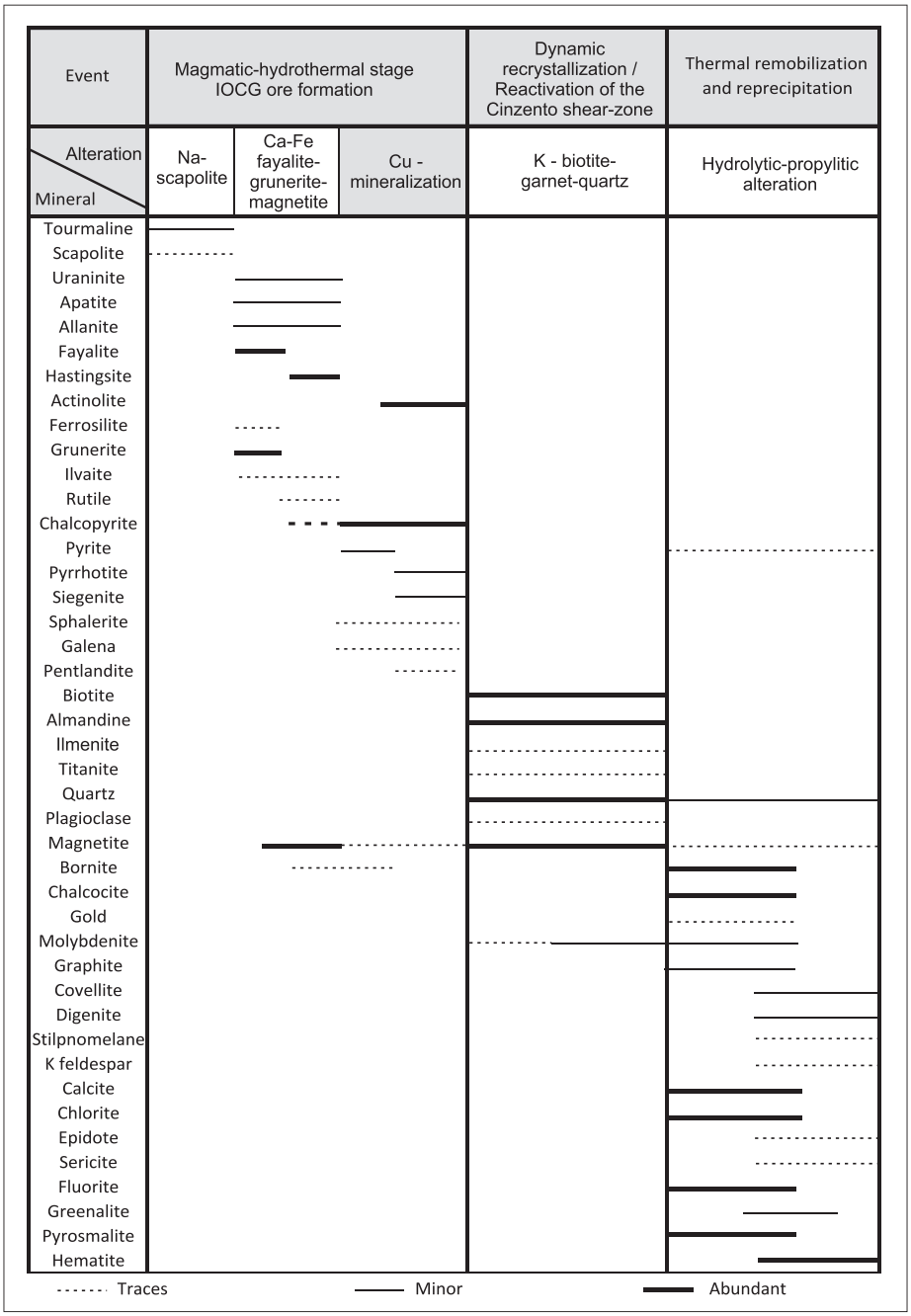

Fig. 2. Paragenetic sequence showing the hydrothermal alteration and mineralization stages of the Salobo deposit. Modified from Valadão (2019).

Magnetite also occurs as inclusion-rich medium-grained grains in the chalcopyrite-matrix of the breccias.

Potassic alteration recognized close to mineralized zones consist of biotite-almandine-quartz-magnetite, which define the mylonitic foliation. Biotite replaces early grunerite and surrounds with pressure shadows almandine porphyroblasts, some of which present fine-grained magnetite inclusions. Quartz display undulose extinction and subgrain formation. It occurs as thin layers and veinlets consistently oriented with the mylonitic foliation and equigranular and granoblastic magnetite grains. Molybdenite, ilmenite, and apatite are common accessory minerals.

The last hydrothermal assemblage consists of chlorite alteration and calcite-fluorite-bornite-chalcocite-digenite veins, representing the remobilization of previous Cu-ore (chalcopyrite). These veins infill fractures that crosscut magnetite-rich schist. Fluorite also occurs as xenoblastic crystals associated with magnetite, bornite, chalcocite, biotite, chlorite, and calcite. Chalcopyrite is less common and occurs as crosscutting veins in magnetite-rich zones. Bornite-digenite-chalcocite association show myrmekitic-symplectic textures. This alteration type includes besides later low-temperature assemblage that overprints previous stages and is represented by stilpnomelane-greenalite-pyrosmalite-hematite. Needle-shaped crystals of stilpnomelane crosscut chalcocite-bornite, while pyrosmalite forms subidioblastic crystals between them. Hematite is observed as veinlets associated with calcite and selective replacements of almandine and magnetite.

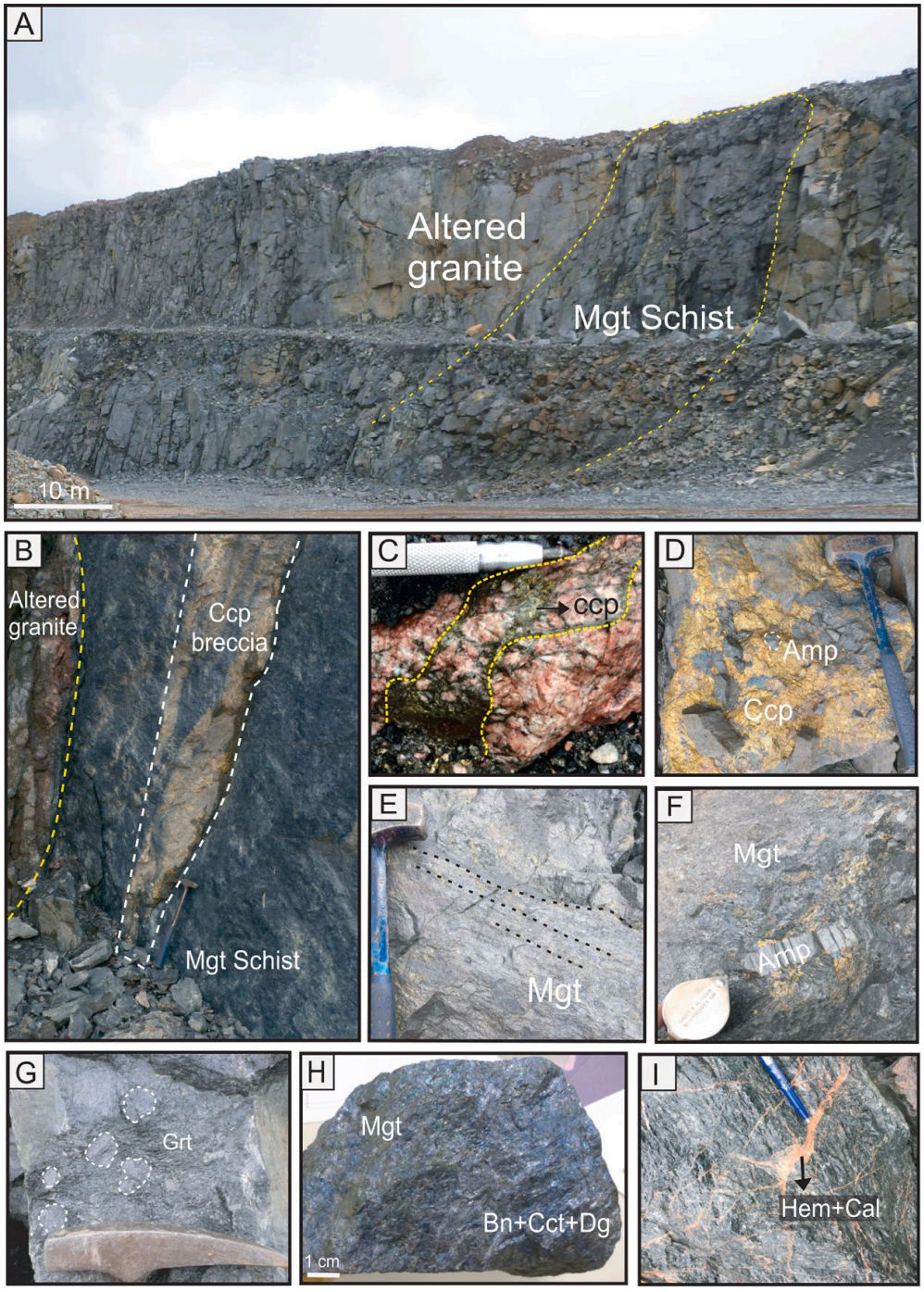

Fig. 3. Sections through the giant Salobo mining area showing (A) the domains with different rheology of the hydrothermal altered granitic rocks and magnetite schists rocks (ductile); (B) preserved sub-vertical lens-shaped chalcopyrite breccia between magnetite-schists. Macroscopic ore samples: (C) Granitic rock with hydrothermal alteration and chalcopyrite veins. (D) Matrix supported hydrothermal chalcopyrite breccia with clasts of magnetite and amphibole. (E) Magnetite-rich schist with orientated chalcopyrite. (F) Magnetite breccia with amphibole grains surrounded by chalcopyrite. (G) Garnet-biotite schist. (H) Magnetite schist with Cu-sulfide ore including bornite, chalcocite and digenite. (I) Hemtatite + Calcite veins cross-cutting the foliation of the magnetite-rich schist. *Abbreviations: Amp: amphibole. Bn: bornite. Cal: Calcite. Ccp: Chalcopyrite. Cct: chalcocite. Dg: digenite. Grt: granite. Hem: hematite. Mgt: Magnetite.*

3. Material and methods

We have studied a suite of open-pit samples (n = 30) collected from the Salobo Mine, (approximate sample location is indicated in Fig. 1B). The sample-set comprises granitic rocks with hydrothermal alteration (SLB 101–102; Fig. 3A, B, C), chalcopyrite and magnetite hydrothermal breccias (SLB 103–104, SLB 1–7; Fig. 3D), magnetite-rich schists (SLB 105–107, SL 1–2; Fig. 3E, F, H, I) and garnet-biotite schists (SLB A-C; Fig. 3G). The granite and chalcopyrite breccias are exposed in meter-scale, low-strain sigmoidal microlithons within the mylonitic fabric (Fig. 3A, B).

Petrographic descriptions under transmitted and reflected light microscopy were carried out on forty polished-thin sections to recognize the ore mineral assembly, textural relationships, microinclusions, and possible chemical zonation within magnetite.

The mineral chemistry analyses were obtained using a 5-spectrometer JEOL JXA-8230 SuperProbe electron probe microanalyzer (EPMA) at the University of Brasília (Brazil). The wavelength dispersive (WDS) analyses were performed at an accelerating voltage of 15 kV, sample current of 10nA, and electron beam of 10 μm of diameter. Minor and trace elements, such as Si, K, Ca, Al, Ti, Mg, Mn, Cr, V, Ni, and Zn were measured. The counting time was 20 s, except for Zn and Cu 30 s, Mn 40 s, Ni 50 s, and V 60 s. Both synthetic and natural mineral standards patterns of oxides and silicates were used for the analyses, and the same standards and procedures were retained throughout the analytical work. Raw X-ray intensities for all elements were corrected using standard ZAF techniques with the JEOL software. Microprobe results were treated using Excel in-home spreadsheets with adjustments for magnetite following Deditius et al. (2018). The oxygen content was calculated based on the stoichiometric and an ideal AB_2O_4 formula (Droop, 1987). All analyzed EPMA analytical results are listed in Supplementary Data Table A1.

Scanning electron microscope analysis was carried out at the scanning electron microscope equipped with high definition back- scattered electron detector (HDBSD), at the National Institute of Criminalistics, Civil Police D.F. - Brasilia. The operation was under an acceleration voltage of 20 kV and a vacuum of 0.0009 Pa.

Multiple S isotopes (^{32}S, ^{33}S, and ^{34}S) were determinate on pyrite, chalcopyrite, and pyrrhotite from two polished thin sections (i.e., SLB 2A and SLB 7C) representatives of the chalcopyrite hydrothermal breccias samples. The analysis was performed using the NordSIMS Cameca IMS 1270 located at the Swedish Museum of Natural History, Stockholm. Analytical methods and instrument parameters followed are those described by Whitehouse et al. (2005) and Whitehouse (2013). In brief, a primary Cs^+ beam with an incident energy of +10 kV, illumination of ca. 100 μm resulted in a typical beam current of ca. 10–20 nA. The mass spectrometer was operated with a high mass resolution ($M/\Delta M \approx 8000$). Field aperture and mass, with simultaneous detection of three Faraday cup detectors positioned along the focal plane for simultaneous measurement of ^{32}S, ^{33}S, and ^{34}S, operated at an effective high mass resolution of ca. 4500 on the ^{33}S channel. Suitably trimmed sections were mounted together with the laboratory Balmat and Ruttan pyrites, Nifty chalcopyrite, and MV1 pyrrhotite standards for sulfur isotope analyses. Sulfur values are reported in relation to Vienna-Canyon Diablo Troilite (V-CDT). All δ34S isotope values are presented in Supplementary Data Table A2.

4. Results

4.1. Sample description

The following descriptions of the samples provide the main petrographic features and alteration minerals associated with the Salobo deposit's mineralized zones.

4.1.1. Hydrothermally altered granitic rocks

Altered granitic rocks are equigranular, fine- to medium-grained with a granodioritic composition. It is foliated but locally isotropic and commonly displays a pink color in least-altered zones and reddish where hydrothermally altered (Fig. 3C). Plagioclase in the rock is commonly altered with partial to total replacement by scapolite, biotite, and chlorite. Features of shearing are present, such as stretched potassium feldspar, quartz ribbons, besides undulose extinction and subgrain formation in the quartz phenocrysts. Hydrothermal alteration is represented by feldspars sericitization, quartz, and plagioclase interstices filled by chlorite. Apatite, magnetite, allanite, titanite, and carbonates are accessory minerals. Bornite and chalcopyrite interstitial grains are also present with hematite boxwork overgrowths (Fig. 4A).

4.1.2. Chalcopyrite hydrothermal breccia

The polymictic chalcopyrite breccia is greenish-yellow characterized by a ccp-rich matrix (pre-kinematic; Fig. 3D, 5A) preserved within the magnetite schists between the schistosity (Q domains; Fig. 3B). It is composed of sulfide-rich mineralogy of siegenite, pyrite, pyrrhotite, and minor bornite, galena, sphalerite, pentlandite. Pyrite occurs as subhedral fine grains (10–40 μm diameter) and fractured crystals with absorption rims, some of which show chalcopyrite (Fig. 4B) and pyrrhotite replacement (Fig. 4C). Pyrrhotite has an anhedral habit and usually occurs along with contacts of chalcopyrite-matrix and silicate clasts, locally occurs as subhedral grains associated with magnetite (Fig. 4D). Lamellar pentlandite exsolutions are rarely visible at the chalcopyrite matrix.

Clasts are also made up of fayalite, ferrosilite, hastingsite, actinolite, grunerite, hornblende, magnetite, uraninite, apatite allanite; some exhibit alteration to phyllosilicates (chlorite, stilpnomelane, Fe-pyrosmalite, greenalite) and oxides (hematite). The clasts size varying from ~0.1 cm up to 3 cm clasts and present rounded to sub-angled shapes. Magnetite occurs both with filled fractures and borders of actinolite and inclusion-rich grains (Fig. 4E). Accessory apatite was classified as chlorapatite, with a Cl content of 2.04–4.56 wt% and an average F content of 0.05 wt%.

4.1.3. Magnetite hydrothermal breccia

The matrix displays a gradual transition from chalcopyrite to magnetite cementation (subordinate magnetite breccia domains; Fig. 5) in some portions of the chalcopyrite breccia, in which fayalite, ferrosilite, hastingsite, and less abundant grunerite were identified. This magnetite-matrix phase presents dark grey tones and is characterized by amphibole clasts and interstitial chalcopyrite and bornite grains close to the iron-rich silicates grains both not larger than ~50 μm (Fig. 5C, D). the texture also shows incipient foliation and clast alignment, especially in zones with less chalcopyrite-matrix content.

4.1.4. Magnetite schist – (magnetitite)

The magnetite breccia domain progressively transitions to magnetite schists, which are dark grey, fine- to medium-grained, granoblastic to mylonitic rocks (Fig. 3E, F, H, I). The magnetite schist is composed of magnetite, with minor biotite, amphibole, quartz, and altered garnet. Magnetite-rich domains (magnetitite) up to 80 to 90% consist of composite layers of magnetite porphyroblasts (~50–100 μm). The foliation is locally observed and marked by magnetite's preferred orientation (Fig. 4F, G). Graphite and lepidoblastic-deformed molybdenite (Fig. 4H) occur parallel to the schist foliation.

The granoblastic texture and tectonic foliation are cut by at least two directions of brittle veins of bornite- digenite- chalcocite, fluorite, and calcite (Fig. 4I). Minor amounts of chalcopyrite also occur in discordant veins (Fig. 4F). Bornite is also present as interstitial grains and filling fractures in magnetite grains. It occurs with myrmekitic-symplectic textures and exsolutions with chalcocite, digenite, and covellite (Fig. 4H). Some porphyroblasts of magnetite (>100–700 μm) present ilmenite exsolutions of microns wide (<10 μm) and show a classic trellis

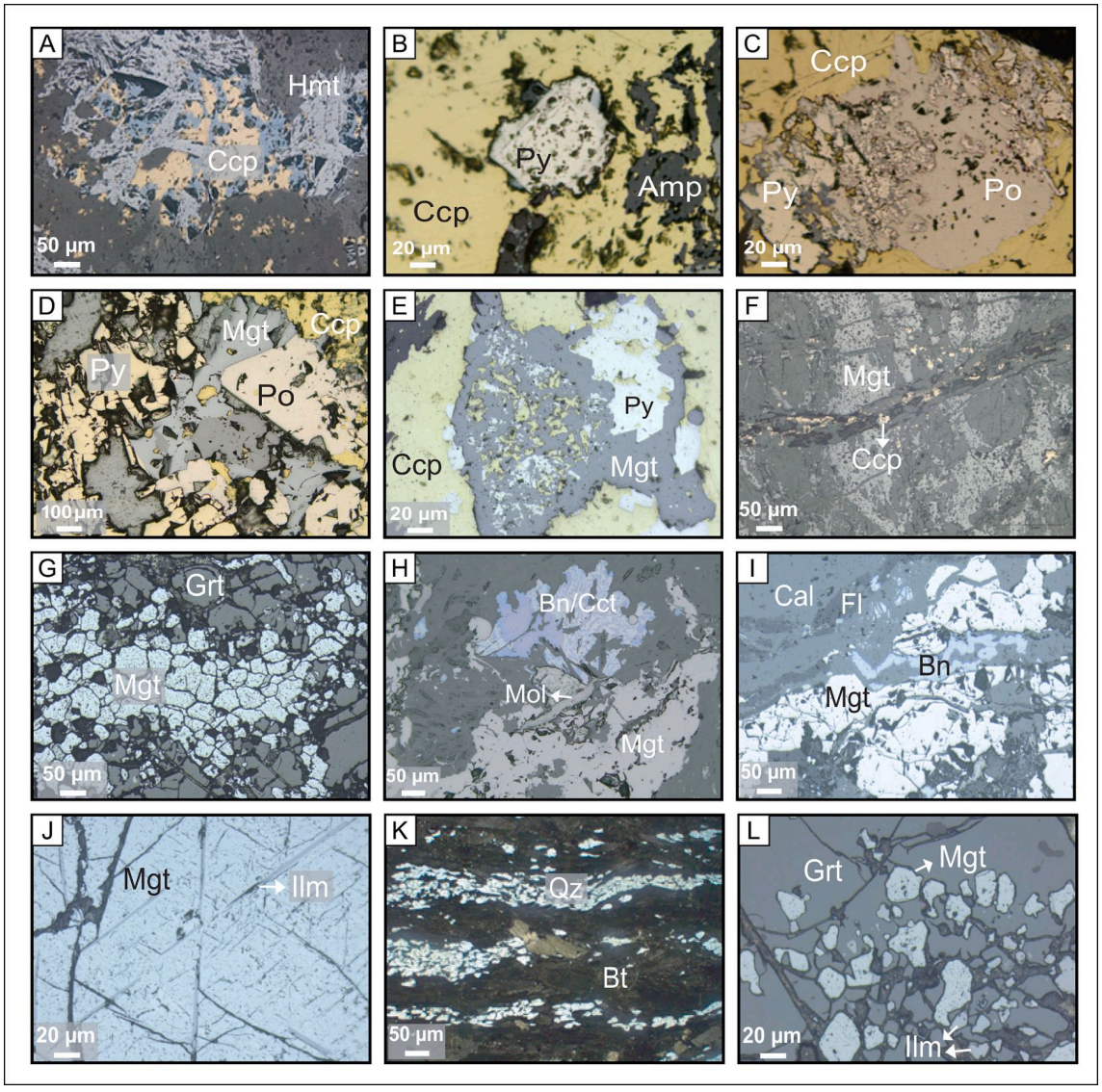

Fig. 4. Micro-photographs of representative thin sections showing textures from *hydrothermal altered granitic rock* (A), *chalcopyrite breccia* (B, C, D and E), *magnetite-schist* (F, G, H, I and J) and *garnet-biotite schist* (K and L). (A) Boxwork hematite overgrowth on interstitial bornite and chalcopyrite. (B) Massive chalcopyrite with subhedral pyrite grain showing an alteration rim. (C) Pyrite crystal transforming to pyrrhotite in a chalcopyrite matrix. (D) Subhedral pyrrhotite associated to pyrite and magnetite in the chalcopyrite matrix. (E) Inclusion-rich magnetite associated to pyrite in the chalcopyrite matrix. (F) Bands of magnetite and amphibole with interstitial chalcopyrite. (G) Granoblastic magnetite associated with almandine. (H) Bornite in myrmekitic-symplectic textures with chalcopyrite, and molybdenite lamellae associated with magnetite. (I) Veins with calcite, fluorite and bornite crosscutting granular-massive magnetite. (J) Ilmenite exsolutions in classic trellis structure, regularly distributed along with three directions in magnetite. (K) Biotite- and quartz-rich intercalated bands forming the rock schistosity. (L) Magnetite and ilmenite interstitial grains in garnet. *Abbreviations: Bn: Bornite. Cal: Calcite. Cct: Chalcocite. Ccp: Chalcopyrite. Fl: Fluorite. Grt: Garnet. Hmt: hematite. Ilm: Ilmenite. Mgt: Magnetite. Mol: Molybdenite. Qz: quartz. Note: K in transmitted light.*

structure, regularly distributed along with three directions (Fig. 4J). Accessory apatite was classified as fluorapatite with an average F content of 3.4 wt%.

4.1.5. Almandine-biotite schist

The almandine-biotite schists are dark green, fine- to coarse-grained, lepidoblastic, intensely foliated, and porphyroblastic rocks (Fig. 3G). These rocks are composed of almandine porphyroblasts embedded in a matrix of biotite, quartz with minor plagioclase, apatite, chlorite, and amphibole. An anastomosing spaced schistosity pattern is formed by the main foliation planes, which is marked by aligned millimetric to centimetric (up to 4 cm) bands of biotite and quartz (Fig. 4K). Lepidoblastic biotite is partially chloritized. Almandine porphyroblasts (up to ~10 cm diameter) are commonly rotated and surrounded by biotite and quartz, forming well-developed pressure shadows indicating rotation and growth under shear. Almandine also displays helycitic inclusions trails of quartz, magnetite, ilmenite, and biotite (Fig. 4L).

4.2. Magnetite textures

In view of the texture, occurrence, and mineral association three main types of magnetite associated with the main hydrothermal alteration stages were recognized in the Salobo mineralization and host rocks. No marked oscillatory zoning is observed in SEM-BSE (backscattered electron) images of any of the abovementioned magnetite types. The key textural and mineral relationships are summarized in Table 2.

Magnetite type I - Coarse-grained primary magnetite I is subhedral to anhedral with a grain size of 0.1 to 2 mm (Fig. 6A, B, C – 7A). This magnetite presents a massive habit and is commonly enclosed in or

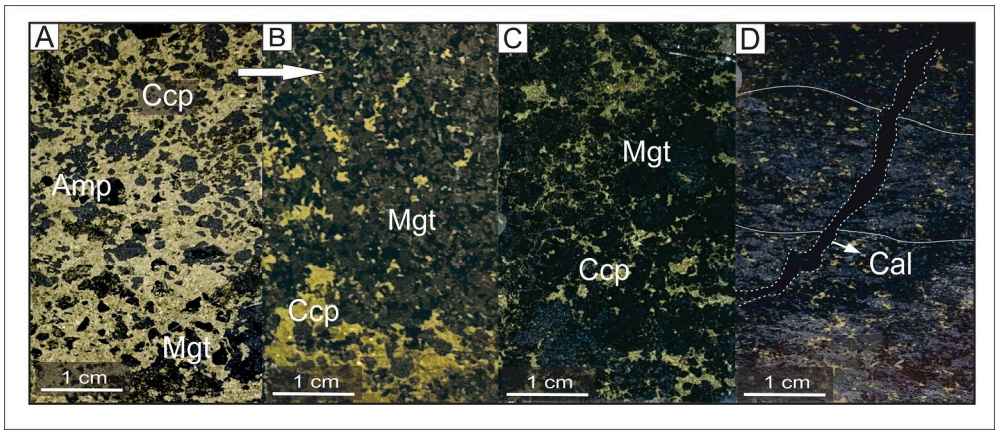

Fig. 5. Photos of polished thin sections showing a gradual change in the matrix composition and rock texture of the hydrothermal breccias from fresh massive chalcopyrite-matrix (A) to more deformed magnetite-matrix (C). (A) Chalcopyrite breccia with subhedral magnetite and amphiboles grains. (B) Polished thin section showing the gradual change between magnetite-matrix breccia to chalcopyrite breccia. (C) Matrix supported magnetite breccia with chalcopyrite. (D) Magnetite-rich schist with interstitial chalcopyrite grains cut by a discordant vein of calcite. *Abbreviations: Amp: amphibole. Cal: Calcite. Ccp: Chalcopyrite. Mgt: Magnetite.*

Table 2
Summary information of magnetite types from the IOCG Salobo deposit.

Magnetite Type	Magnetite textures	Important Associated minerals		Mineral Inclusions in Mgt	Rock type	Temperature	
		Sulfides oxides	Gangue mineralogy			Hydrothermal alteration	Mgt geothermometry
Type I	Massive Granular	Ccp, Bn	Hst, Fs, Fa	Mnz, Ap	Ccp breccia – Mgt breccia	Ca-Fe	~515 °C ± 50 °C
Type II	Granular	Py, Po, Pn	Act, Amp	Mnz, Zrn, Urn, Ap, Ccp, Bn, Py	Ccp breccia	Fe-enrichment	~490 °C ± 50 °C
Type III	Granoblastic	Hem, Bn, Cv, Cct, Dg veins Mol, Ilm	Fl, Cal veins Bt, Qz, Alm	Inclusion-poor	Mgt-rich schist – almandine-biotite schist	Bn exs – Sulfur remobilization Potassic-Chloritization	~470 °C ± 50 °C

Note: Mineral abbreviations = Act: actinolite, Alm: almandine, Amp: amphibole, Ap: apatite, Bn: bornite, Bt: biotite, Cal: calcite, Ccp: chalcopyrite, Cct: chalcocite, Chl: chlorite, Cv: covellite, Dg: digenite, Fa: fayalite, Fs: ferrosilite, Fl: fluorite, Gr: graphite, Grt: garnet, Hst: hastingsite, Hem: hematite, Ilm: ilmenite, Mgt: magnetite, Mnz: monazite, Mol: molybdenite, Pn: pentlandite, Po: pyrrhotite, Py: pyrite, Qz: quartz, Urn: uraninite, Zrn: zircon. Exs: exsolutions.

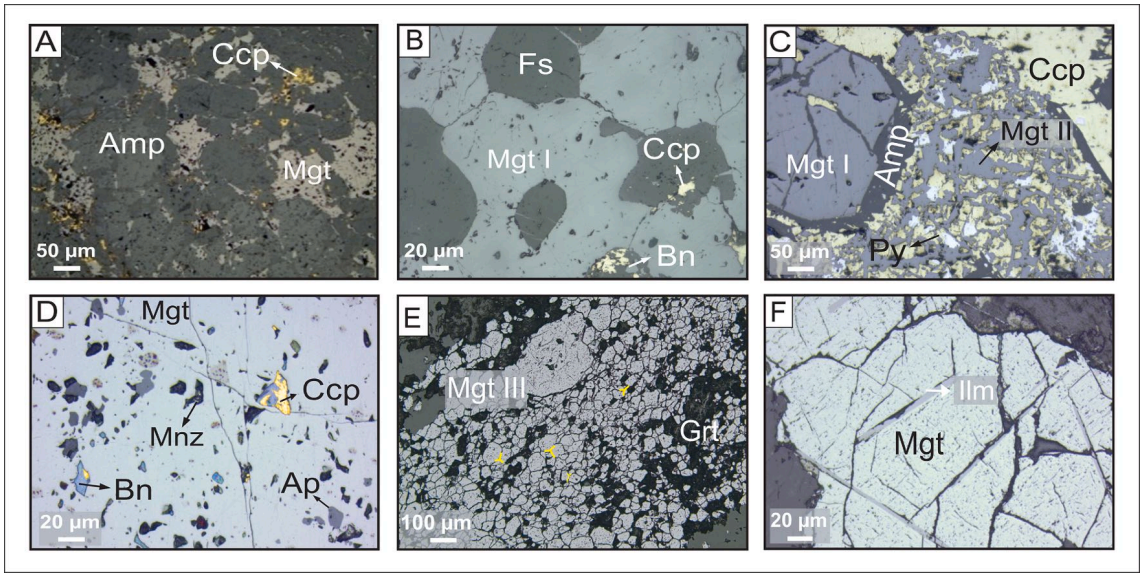

Fig. 6. Micro-photographs of the magnetite occurrences and its principal textures. (A) Massive magnetite associated with amphibole and disseminated chalcopyrite. (B) Pristine-massive magnetite associated with ferrosilite and interstitial chalcopyrite and bornite. (C) Magnetite grain (Mgt I) close to amphibole and pyrite-chalcopyrite assemblage in pre-existing magnetite (Mgt II). (D) Magnetite with inclusions including bornite, chalcopyrite, monazite and apatite. (E) Porphyroclast of magnetite with ilmenite exsolutions (*in* Fig. 6*F*), granular magnetite III with 120° triple junctions (*yellow* lines) and garnet and ilmenite grains. (F) Ilmenite exsolutions following crystallographic planes. *Abbreviations: Amp: Amphibole. Ap: Apatite. Bn: Bornite. Ccp: Chalcopyrite. Fs: Ferrosilite. Ilm: Ilmenite. Mgt: Magnetite. Mnz: Monazite. Py: Pyrite.* (For interpretation of the references to color in this figure legend, the reader is referred to the web version of this article.)

marginal to fayalite, ferrosilite, and hastingsite (Ca-Fe alteration). Some magnetite grains exhibit veins and borders of actinolite (Fig. 6C – 7A) and contain monazite and apatite inclusions, both no larger than 8 µm diameter. SEM-BSE imaging did not reveal any secondary textures.

Magnetite type II- Subhedral magnetite grains present in the matrix-supported hydrothermal chalcopyrite breccia (Cu-Au mineralization)

represent the magnetite II (Fig. 6C, D – 7B). Grain size ranging from ~0,3 to 8 mm in diameter. Magnetite II often occurs close to the Mgt I and grains/fragments of amphibole. One of the striking features observed in magnetite II is randomly distributed inclusions, varying from 3 to 60 μm in diameter. Typical mineral inclusions consist of monazite, zircon, uraninite, apatite, amphibole, and Cu-Fe sulfides, including pyrite, bornite, and chalcopyrite (Fig. 6D – 7B).

Magnetite type III - Equigranular and granoblastic magnetite type III is related to the magnetite-rich schists (Potassic alteration; Fig. 4G). Magnetite grains occur parallel to the schist foliation in contact with ilmenite, showing recrystallization features such as foam texture with well-defined 120° triple junctions (Fig. 6E – 7C, D) and interconnected microscope-scale porosity (Fig. 7E, F). Overall, the grain size is no larger than 100 μm diameter. However, some porphyroblast (>100–700 μm) are also present (Fig. 6E). Magnetite III typically does not show exsolutions, except for the magnetite porphyroblasts, which occurs with ilmenite oxy-exsolution (Fig. 6F).

4.3. Magnetite geochemistry

Full EPMA results for magnetite types are presented in Supplementary material Table A1, and averages values of magnetite composition are in Table 3. Fig. 8A shows comparative box and whisker diagrams of minor and trace elements between magnetite types. Magnetite grains from all samples have Fe contents ranging from 67.32 to 72.19 wt%, lower than the stoichiometric value of 72.4 wt%. Different magnetite types show different Fe contents. Mgt III has higher iron contents (ave 71.98 wt%) than Mgt I and II (ave 70.01 wt% and 71.51 wt%, respectively).

In general, the minor and trace elements contents for the magnetite types varying from below detections limits to ~2 wt% (Fig. 8A). Broadly, the three magnetite types have a similar concentration in Si and Mn, varying from 0.01 to 2.02 wt% Si and 0.01 to 0.09 wt% Mn. Besides, the concentration of K is remarkably homogeneous, varying from 0.01 to ~0.02 wt% in Mgt II and Mgt III, except for Mgt I, in which K content is

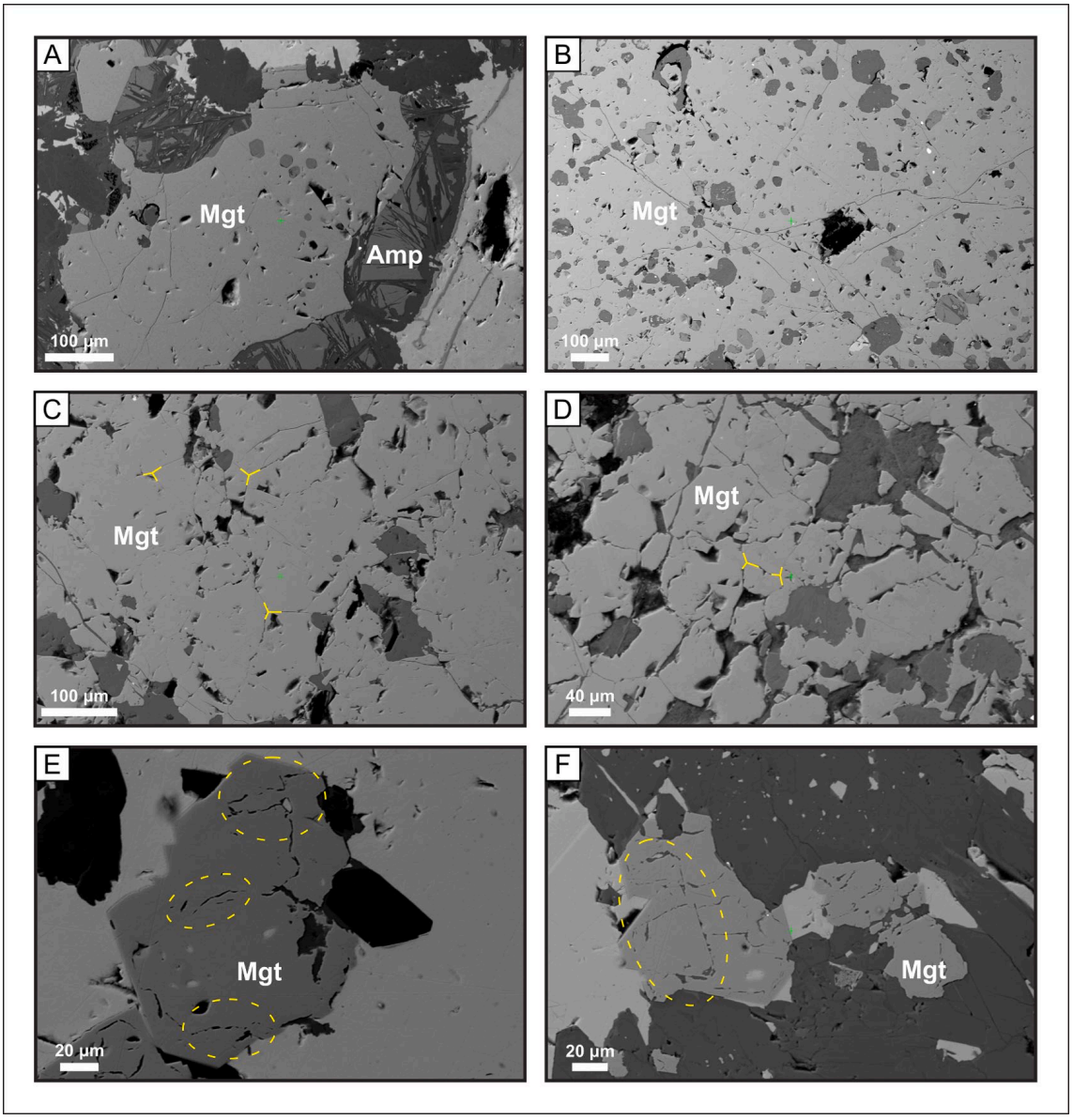

Fig. 7. Back-scattered electron images of magnetite textures. (A) Granular magnetite (Mgt I) with some inclusions and surrounded by fragments of amphibole. (B) Inclusion-rich magnetite (Mgt II). Granoblastic magnetite (Mgt III) in foam texture with 120° triple junctions (*yellow* lines) (C, D) and interconnected micro porosity (*yellow circles*) (E, F). Non distinct zonation was observed. *Abbreviations: Amp: Amphibole. Mgt: Magnetite.* (For interpretation of the references to color in this figure legend, the reader is referred to the web version of this article.)

Table 3
Summary of the entire chemical data of trace element composition of magnetite occurrences (Mgt I, II and III) by EPMA analyses. The corresponding graphic is shown in Fig. 8A. Total data is available in Supplementary material Table A1.

Magnetite	Element	Fe	Si	K	Ca	P	Al	Mn	Mg	Ti	Zn	V	Ni	Cr
Type I	Min	67,324	0,014	0,016	0,018	0,014	0,008	0,040	0,008	0,046	0,019	0,015	0,039	0,040
	Ave	71,016	0,144	0,033	0,091	0,028	0,137	0,065	0,047	0,107	0,593	0,036	0,054	0,052
	Max	72,193	2,025	0,050	0,268	0,049	0,555	0,091	0,175	0,297	1,654	0,123	0,079	0,066
Type II	Min	67,017	0,015	0,018	0,018	0,012	0,015	0,049	0,007	0,053	0,066	0,014	0,037	0,036
	Ave	71,507	0,111	0,028	0,027	0,025	0,159	0,086	0,023	0,169	1,055	0,040	0,046	0,052
	Max	72,975	0,208	0,027	0,034	0,026	0,399	0,092	0,035	0,352	1,915	0,101	0,128	0,096
Type III	Min	70,294	0,041	0,020	0,016	0,015	0,051	0,012	0,007	0,074	0,026	0,015	0,032	0,040
	Ave	71,981	0,077	0,024	0,020	0,021	0,193	0,062	0,014	0,177	0,940	0,049	0,065	0,070
	Max	72,975	0,208	0,027	0,034	0,026	0,399	0,092	0,035	0,352	1,915	0,101	0,128	0,096

Note: All concentrations are reported in wt%. Total analyses (n) = 107.

slightly higher, 0.01 to 0.05 wt%. Unlike the previous elements, the concentration of Zn in the three magnetite types vary over a relatively wide range from 0.01 to 1.92 wt% (Table 3; Fig. 8A), which may be due to some undetected Zn-bearing inclusions during EPMA analysis.

Magnetite type I has Ca, P, Mg, and Ni contents of 0.01 to 0.05 wt%, 0.01 to 0.27 wt%, <0.01 to 0.17 wt%, and 0.04 to 0.078 wt%, respectively, higher than Mgt type II and III (Fig. 8A). Magnetite type II does not show significantly higher or lower contents in comparison with the other types. Magnetite type III shows Al, Ti, V, and Cr contents (0.5 to 0.39 wt%, 0.07 to 0.35 wt%, 0.01 to 0.10 wt%, and 0.04 to 0.09 wt%, respectively) higher than Mgt I and Mgt II. Despite the limited data for K, P, and Ni contents in magnetite III, there is likely a trend toward higher Ni (0.03–0.12 wt%) and lower K (0.02–~0.3 wt%) and P (0.01–0.02 wt %) contents in mgt III (Fig. 8A). Moreover, both Mgt I and Mgt II have lower Al, Ti, and Cr contents than Mgt III, and the K, P, M,g, and Ni contents show a decrease from Mgt I to Mgt III.

The application of geothermometry in magnetite from the Salobo deposit aimed to estimate the formation temperature of each magnetite type, according to the Mg-content empirical geothermometer (Canil and Lacourse, 2020). Despite, different calibration results in different temperatures and the misfit of temperature within ±50 °C, there is a contrast between the magnetite types and their approximated temperature: early Mgt I has a relatively higher temperature interval, which varies between 447 and 642 °C; than those calculated for Mgt II (439 to 592 °C) and Mgt III (439 to 525 °C) (Table 4; Fig. 8B). The highest calculated temperature (~642 °C) corresponds to magnetite with both fractures and rims of amphibole in the chalcopyrite-breccia matrix (similar to Fig. 6C).

4.4. Sulfides and sulfur isotope data

Chalcopyrite, pyrrhotite and pyrite grains from the chalcopyrite breccia were analysed for sulfur isotopes. The samples contain variable proportions of pyrite, chalcopyrite, pentlandite, pyrrhotite, bornite, chalcocite and digenite. Representative mineral textures of Cu-(Fe) sulfides in the chalcopyrite hydrothermal breccia are depicted in Fig. 4B-E.

Chalcopyrite constitutes the main and one of the first minerals to crystallize in the sulfide phase. A variety of different chalcopyrite types is present; however, two principal generations were analysed. The first one (Ccp 1) corresponds to the massive breccia matrix that host pyrite and pyrrhotite (Fig. 4B, E). Locally it is replaced by bornite. The second chalcopyrite populations (Ccp 2) occur as inclusions in magnetite with some intergrowth with pyrite (Fig. 4E, 6C), and locally also with magnetite.

Pyrrhotite forms coeval with chalcopyrite in the matrix. The grains show mainly an anhedral habit with subordinate subhedral occurrences (Fig. 4 C, D). Pyrrhotite forms in close association with silicate clasts (amphibole) and magnetite. Locally, pyrrhotite present a pervasive replacement by pyrite (Fig. 4C) and incipient replacement by pentlandite.

Pyrite occurs in two generations. The first is associated with the chalcopyrite matrix and occurs mainly with subhedral to anhedral habit (Fig. 4B). Textures include replacement by chalcopyrite and pentlandite. Closer inspection of the euhedral grains shows rims of overgrown by later chalcopyrite (Fig. 4B). As same as chalcopyrite, the second pyrite population occurs as inclusions in magnetite intimately intergrowth with chalcopyrite (Fig. 4E). Its habit is conditioned by the cleavage planes of magnetite, thus showing a right angle to anhedral edges.

4.4.1. Sulfur isotopes

The total $\delta^{34}S$ values obtained in pyrite (n = 6), pyrrhotite (n = 14), and chalcopyrite (n = 15) from the Salobo deposit are presented in Supplementary material Table A2. The results are all positive and cluster in a narrow range between 0.88 and 5.04‰ (Table 5; Fig. 9A). Only two points from pyrrhotite present values or data outside of the traditional mass-dependent fractionation (MDF) limit ($\Delta^{33}S = 0 \pm 0.2‰$ from Farquhar and Wing (2003), while all points plotted outside the MDF limits proposed by LaFlamme et al. (2018) (Fig. 9B). Besides, the bulk of sulfide isotope results for the Cu-Fe sulfides of the Salobo deposit vary from values expected for a mantle sulfur source ($\delta^{34}S = 0 \pm 2‰$) to heavier $\delta^{34}S$ values (up to +5.04‰).

The chalcopyrite has $\delta^{34}S$ values ranging from 1.3 to 3.35‰. Chalcopyrite that is texturally associated with pyrite as inclusions in magnetite is referred as Ccp2 and display an evident clustering of the sulfur isotope data with a $\delta^{34}S$ range between 1.3 and 1.74‰. Those values are lower than the values from the chalcopyrite-matrix referred as Cpp1 with $\delta^{34}S$ ratios of 2.35 to 3.35‰. Pyrrhotite has comparative more homogeneous sulfur isotope compositions with $\delta^{34}S$ values between 0.88 and 1.98‰. The $\delta^{34}S$ results of pyrite are the more variable, ranging from 1.70 to 5.04‰. Subhedral pyrite grains of the chalcopyrite matrix (similar to Fig. 4B) have narrower $\delta^{34}S$ values between 1.70 and 2.17‰ than those obtained for two pyrite grains with overgrown and chalcopyrite-pyrrhotite replacement (similar to Fig. 4C), which have slightly higher $\delta^{34}S$ values (3.36 and 5.04‰).

5. Discussion

5.1. Multiple stages of magnetite precipitation – Constraints on the chemical signature

In the discriminant diagram based on the Al, Mn, Ti, and V abundances (Fig. 10), the analyses of the magnetite types (Mgt I, II, and III) from the Salobo deposit plot mainly in the porphyry and IOCG deposits fields irrespective of the magnetite type indicating higher Al + Mn contents (Fig. 10). This distribution designates the participation of a magmatic-hydrothermal fluid during the magnetite genesis, as suggested by Knipping et al. (2015). Therefore, Ti contents and V concentrations (Fig. 8A) of the Salobo magnetite agrees with the high-temperature hydrothermal magnetite origin (<15–3560 ppm Ti and V concentrations < 3380 ppm; Nadoll et al., 2014; Knipping et al., 2015; Nadoll et al., 2015) expected for IOCG deposits. A similar distribution of

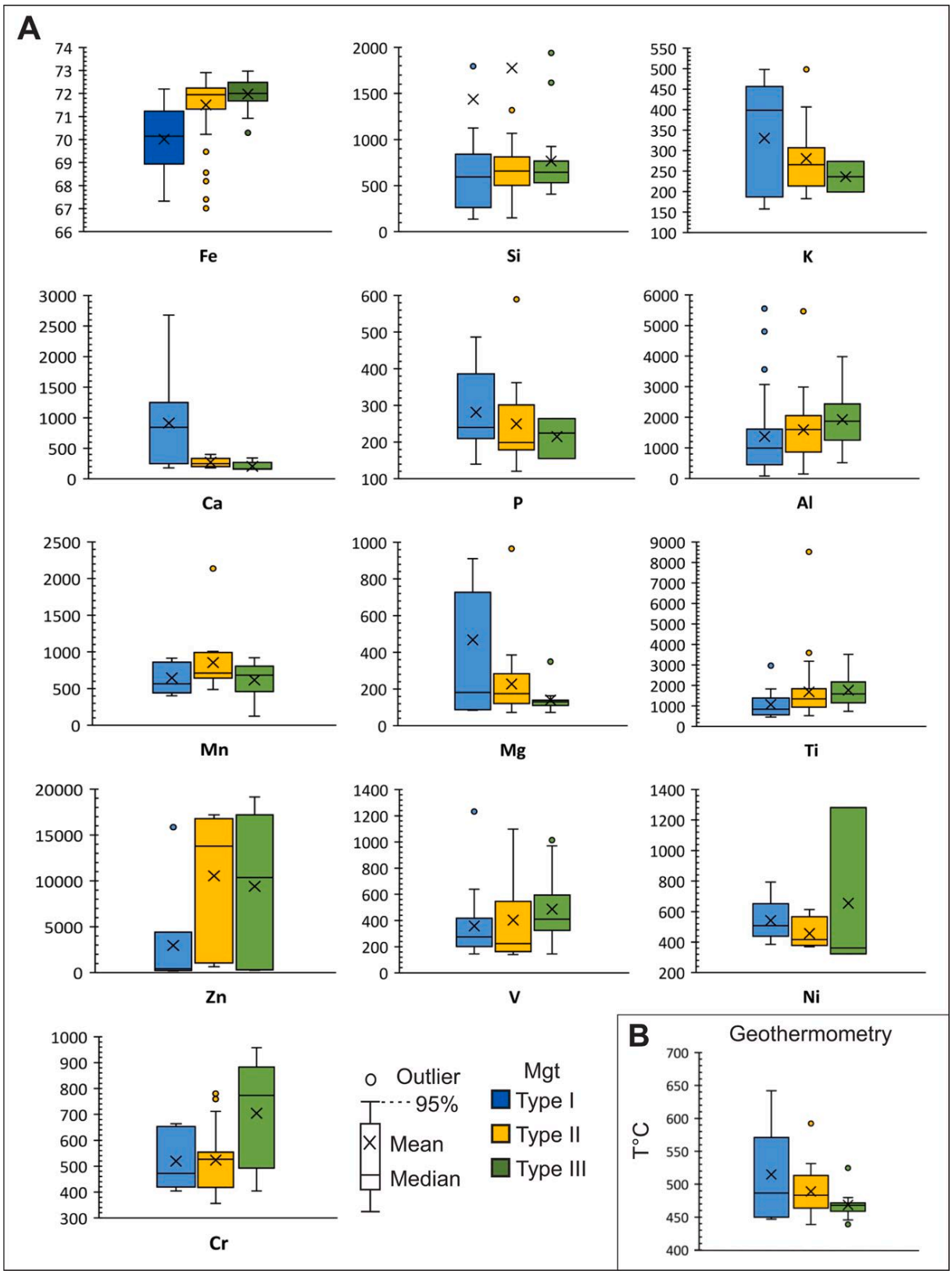

Fig. 8. (A) Data distribution in wt% for Fe and ppm for important minor and trace elements variations of the magnetite types (Mgt I, II and III) in box and whisker plots. (B) Distribution of geothermometry $T_{Mg\ mag}$ for the magnetite types (Mgt I, II and III) based on Canil and Lacourse (2020). The upper and lower margins of the box represent the upper and lower 50 percentile of the data. The whiskers represent the upper and lower threshold values (95 percentile of the data). Mean values are shown as "*x*" and median values as solid black lines. See text for further discussion. Data for magnetite are given in Supplementary Data Table A1.

Table 4
Temperature (°C) estimated using magnetite Mg composition geothermometry (Canil and Lacourse, 2020). The corresponding graphic is shown in Fig. 8B.

Magnetite		Geothermometer (°C) ± 50°								
Type I	Max	642	487	449	591					
	Min	447	486	642	529					
	Ave	515	552	450	447					
Type II	Max	592	483	480	462	480	531	467	524	505
	Min	439	464	464	510	439	439	483	511	516
	Ave	489	592	514	450	513	490	487	443	
Type III	Max	525	439	446	458	466				
	Min	439	470	471	472	464				
	Ave	469	471	480	461	525				

Table 5
Summary data of sulfur isotopic values of chalcopyrite, pyrite and pyrrhotite of the Salobo deposit. The corresponding graphic is shown in Fig. 9. Total values are available in Supplementary material Table A2. 12.

Sample N°	Mineral	$\Delta^{34}S_{V\text{-}CDT}$			±σ (‰)			$\Delta^{33}S$ (‰)			±σ (‰)		
		Min	Max	Ave	Min	Max	Ave	Min	Max	Ave	Min	Max	Ave
SAL7C	Cpy	2.35	3.35	2.73	0.1	0.13	0.11	−0,20	0,03	−0,09	0,12	0,15	0,13
	Py	1.7	5.04	2.7	0.11	0.11	0.11	−0,14	0,04	−0,04	0,12	0,15	0,13
SAL2A	Cpy	1.3	1.74	1.53	0.1	0.14	0.11	−0,19	0,03	−0,08	0,12	0,13	0,12
	Po	0.8	0.14	1.57	0.09	0.11	0.01	−0,29	0,09	−0,11	0,17	0,17	0,17

Note: A total of 35 points were made. All data can be found in the Supplementary material Table A2.

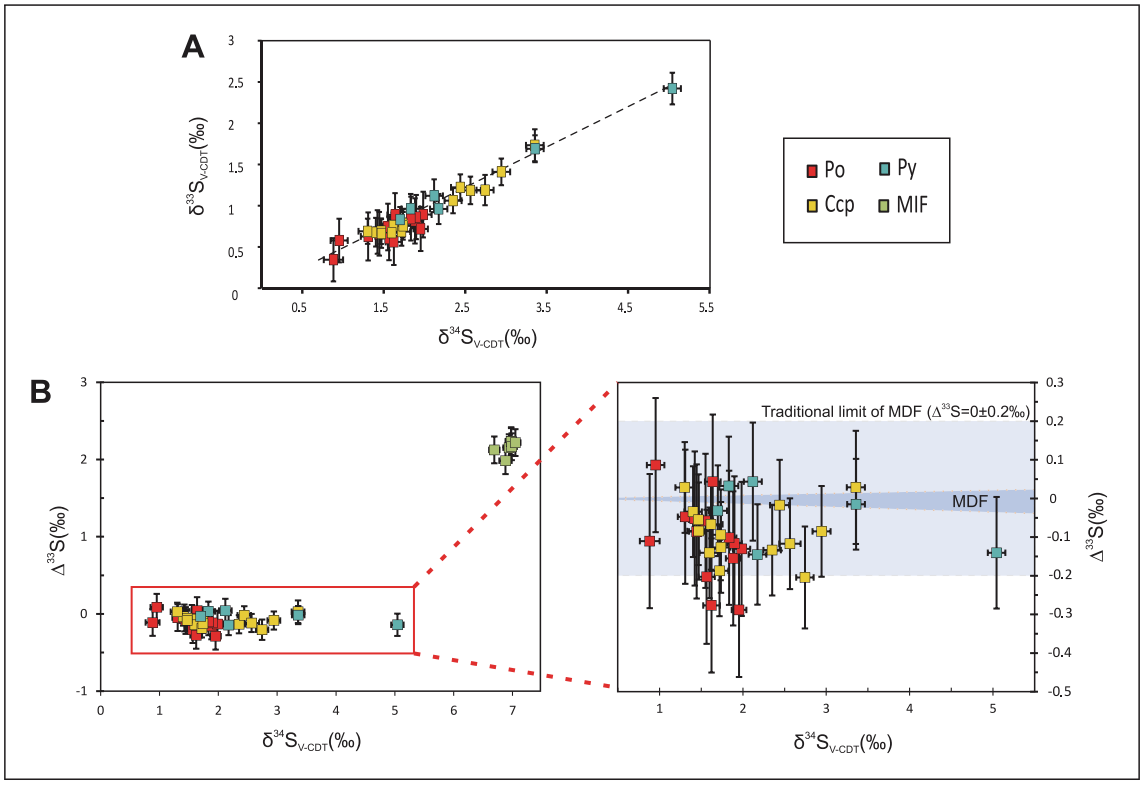

Fig. 9. Diagrams illustrating the distribution of sulfur isotope data of pyrrhotine (po), pyrite (py) and chalcopyrite (ccp) from the Salobo deposit. The data are grouped according to (A) values of $\delta^{34}S_{V\text{-}CDT}$ (‰) vs $\delta^{33}S_{V\text{-}CDT}$ (‰) and (B) values of $\Delta^{33}S$ (‰). MIF (*Mass Independent Fractionation*): Sample pattern of the Swedish Museum of Natural History laboratory, Stockholm (NordSIMS). Grey field delineates the traditional limit of MDF mass-dependent fractionation of sulfur $\Delta^{33}S = 0 \pm 0.2$‰ from Farquhar and Wing (2003) and the orange area delineates the MDF limits proposed by LaFlamme et al. (2018). (For interpretation of the references to color in this figure legend, the reader is referred to the web version of this article.)

these elements can be appreciated in a multielement variation diagram with compilated compositional ranges of magnetite from different deposit types for comparison (Supplementary material – Fig. A1). Broadly, the chemical trend of the three types of magnetite agrees with elements that typify an IOCG deposit geochemical signature, such as Si, Al, Mn, Ti, and V.

Montreuil et al. (2016) showed that each hydrothermal alteration assemblage is associated with distinct element mobility patterns that record the evolving physicochemical properties of the hydrothermal fluid. K and K–Fe alteration is rich in K, Al, Si, whereas Ca–Fe alteration

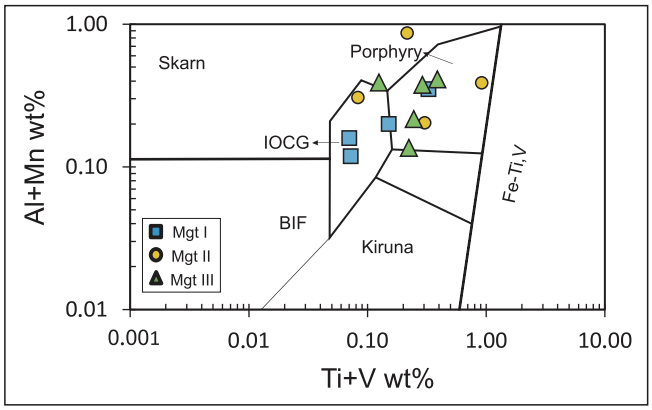

Fig. 10. Al + Mn vs. Ti + V in wt% discrimination diagram proposed by Dupuis and Beaudoin (2011) and modified by Nadoll et al. (2014), showing the composition of the Salobo magnetite (Mgt I, II and III are plotted).

is enriched in Ca, Fe, Mn, Mg, Zn, Ni, and Co. As shown in Fig. 8A, magnetite from the high-temperature Ca–Fe, K–Ca–Fe alteration, and Cu-mineralization (Mgt I and Mgt II) have subtle enrichment in Mg, Mn, K, Ca, and P when compared to magnetite III. That is, the fluids rich in Si, K, Ca, Fe, Mn, Mg, and Zn that form the Ca–Fe alteration (Corriveau et al., 2016; Montreuil et al., 2016) enriched the magnetite I composition in those elements.

In a diagram of (Mn + Mg) vs. (Si + Al)/(Mn + Mg) proposed by Deditius et al. (2018), a subtle distribution can be observed. The magnetite at Salobo decreases in (Mn + Mg) contents while it is enriched in (Si + Al) (Figs. 11, 8A). In detail, the magnetite II and III show an affinity to the late hydrothermal zone, consistent with an origin related to latest hydrothermal stages signed by almandine-biotite schist for magnetite III. This differing trend indicates that at least the Mgt III formed via different mechanisms, however with an origin from the same magmatic fluid of Mgt I and II. Assuming that Mgt type III underwent different conditions during the magnetite evolution; the geochemical difference in Mgt III (i.e., Si, K, P, Mg, Ni, Cr, and Zn) could be linked to processes related to superimposed hydrothermal alteration events recorded in the Carajás Province and thus, in the Salobo deposit (e.g., metamorphic-deformational events and plutonic felsic intrusions at ca. 2.5 and 1.88 Ga; respectively) (Lindenmayer and Teixeira, 1999; Requia et al., 2003; Tassinari et al., 2003; Tavares et al., 2018; Bernard Prado et al., 2019; de Melo et al., 2019; among others). Another evidence of chemical differentiation of Mgt III, is the associated accessory apatite, classified as fluorapatite differing from the apatite inclusions of Mgt II, which is Cl-apatite.

Huang and Beaudoin (2019) showed that magnetite formed by different CDR (Coupled Dissolution-Reprecipitation) presents subtle

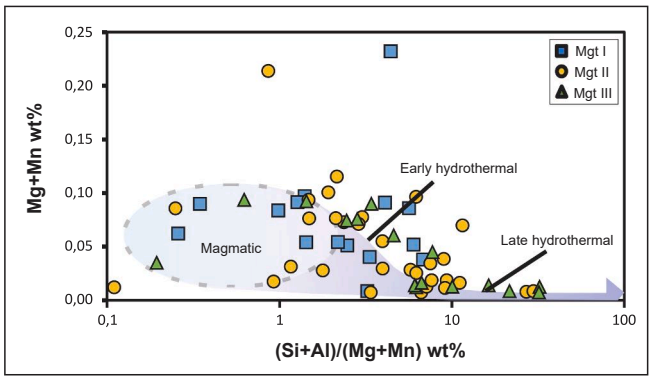

Fig. 11. Mg + Mn vs. (Si + Al)/(Mg + Mn) in wt% plot proposed by Deditius et al. (2018), showing the Salobo magnetite (Mgt I, II and III) composition.

differences in the chemical compositions compared to the parent magnetite. In this perspective, CDR processes could have excluded elements, such as Si, Ca, K, Al, Mn and Mg from primary magnetite (i.e., Mgt I and II), and then forming secondary magnetite variety (i.e., Mgt III), ergo, the CDR results in the same mineral, but with subtle geochemical differences (Harlov et al., 2011; Hu et al., 2014; Ruiz-Agudo et al., 2014). Besides, the local geologic conditions, variations in temperature, pressure and oxygen fugacity, may facilitate the dissolution reaction, thus fluid-assisted processes with the dissolution of primary magnetite result in precipitation of a secondary with Si, Ca and Mg being removed from the primary magnetite during the reactions (Hu et al., 2014; Hu et al., 2015).

Indeed, Mgt III exhibit features attributed to the recrystallization process. For instance, magnetite III grains forms well-developed foliation that follows the schist schistosity, and some grains even show an important evidence of the CDR process, the foam texture with well-defined 120° triple junctions(Fig. 6E – 7C, D) (Urai et al., 1986; Hu et al., 2015; Huang and Beaudoin, 2019). Other features developed during dissolution of magnetite are the pervasive micro-porosities, the formation of interconnected pores in the reaction products and a sharp reaction front between parent and product magnetite (Hu et al., 2014; Huang and Beaudoin, 2019). Magnetite III also shows some of these textures. Several grains display porosity development within the mineral with few interconnected microscope-scale porosity (Fig. 7E, F), however, lacking a sharp contact. The absence of observable sharp reaction interface between parent and product magnetite (i.e., Mgt III) could be attributed to the local geology conditions. Considering the superimposition of hydrothermal alteration in Carajás, the evolving fluid reactions and multiple deformation events may affect the magnetite formed by CDR, and thus, obliterate any relict of sharp reaction interface.

Moreover, the distinct composition in Fe, Mg, Si and K between magnetite types suggest that later hydrothermal overprint may have leached those elements during CDR and promote local distribution of previously locked elements in the early-formed magnetite (i.e., Mgt I and II). This result in the apparent enrichment of those elements in Mgt III (Fig. 8A). It is therefore that the textural data presented here suggest that CDR process may have play an important role in the development of hydrothermal magnetite that host the upgrade Cu-ore in the Salobo deposit, which has not been adequately considered in previous genetical models.

Conversely, some Mgt III grains occur with ilmenite lamellas in distinct crystallographic planes (Fig. 6F). Ilmenite exsolutions are commonly interpreted as a result of oxy-exsolution processes typical of magmatic magnetite, accompanied by a local redistribution of Ti and other elements (Wang et al., 2012; Hu et al., 2015; Huang and Beaudoin, 2019), in contrast, this texture can also be formed by dissolution-reprecipitation processes assisted by fluid-assisted reequilibritation. The latter is more feasible for Mgt III, which may have originally formed at temperatures as high as Mgt I and II (~600 °C, Table 4) both with higher Mg content that was re-equilibrated by later hydrothermal events. For instance, de Melo et al. (2019) proposed that the hydrothermal-metallogenetic event at ca. 2.57 Ga overprinted an older type of copper mineralization and Tassinari et al. (2003) suggested reprecipitation (epigenetic mineralization) caused by the tectonic reactivation episodes related to the Cinzento shear zone evolution and the intrusion of the Old Salobo Granite both at ca. 2.5 Ga. Therefore, Mgt III has undergone a combination of oxy-exsolution and subsequent multiple CDR processes, with the precursor magnetite being modified or destroyed.

In summary, we suggest that Mgt III present a magmatic-hydrothermal origin with an evolution that includes processes of recrystallization and reprecipitation because of intense syn-shearing metasomatism, probably induced by later dynamic recrystallization and magmatic-hydrothermal events recorded at the Salobo deposit.

5.2. A magmatic-derived sulfur source and the effects of magnetite precipitation

The Cu-Fe sulfides from the Cu-mineralization stage at Salobo deposit (chalcopyrite breccias) yielded positive $\delta^{34}S_{V\text{-}CDT}$ values between 0.88 and 5.04‰, suggesting a magmatic sulfur source (Rye, 1993; Schlegel et al., 2017). These values are slightly higher and the variation is wider when compared to $\delta^{34}S_{V\text{-}CDT}$ values between −0.49‰ to +1.63‰, obtained by de Melo et al. (2019) and Santiago et al. (2021) (Table 1) for Cu-sulfides from the magnetite-rich schist. Processes related to sulfide precipitation and sulfide co-crystallization with oxides would elucidate the reason for the sulfur isotopic variations at the same deposit.

For instance, presuming an initial magmatic value of 0‰ for the bulk sulfur isotope composition ($\delta^{34}S_{Bulk}$), sulfides with positive $\delta^{34}S$ values indicate either a shift in the initial $\delta^{34}S_{Bulk}$ value or addition of sulfur derived from a source with higher $\delta^{34}S$ values, which in turn can be explained by the small isotopic gradient during sulfide crystallization or by sulfur disproportionation process (Schlegel et al., 2017). The isotopic grouping of the $\delta^{34}S$ data for chalcopyrite, namely, Ccp 1 (ccp inclusions and grains, mean $\delta^{34}S = 1.56$‰, $\sigma = 0.12$) and Ccp 2 (ccp matrix, mean $\delta^{34}S = 2.73$‰, $\sigma = 0.11$; Fig. 9) suggest an isotopic gradient. The isotopic gradient at the Cu-Fe sulfides deposition site means that part of the chalcopyrite formation could have been driven by a reaction of an oxidized Cu-rich fluid with co-precipitating or previous sulfides which leads to slightly higher isotope values (Rye, 1993). Schlegel et al. (2017), showed that the $\delta^{34}S$ values of chalcopyrite can be partly inherited from the associated pyrite during a Cu-mineralization event. According to the chalcopyrite-pyrite textures, part of the chalcopyrite formation could have been driven by a reaction of pyrite with an oxidized Cu-rich fluid resulting in pyrite replacement (Eq. (1); Schlegel et al., 2017):

$$2FeS_2 + Cu^{2+} + 8H_2O = CuFeS_2 + Fe^{2+} + 2SO_4^{2-} + 4H^+ + 6H_2 \quad (1)$$

Following this rationale, the $\delta^{34}S$ values of Ccp 2 could have been affected by the precursor pyrite with a more positive sulfur isotope signature than the Ccp 1, according to the observed textural replacement of pyrite by chalcopyrite. Moreover, the $\delta^{34}S$ values of the pyrite could have been affected during the replacement, yielding more positive sulfur isotope values for pyrite and Ccp 2 (i.e., 3.36 and 5.04‰).

Likewise, as shown by Schlegel et al. (2017), a wide range of $\delta^{34}S_{V\text{-}CDT}$ values in sulfur from a single source may be generated by closed system isotopic fractionation through magmatic sulfur disproportionation or Rayleigh fractionation processes (e.g., –33.5‰ to 29.9‰; Prominent Hill, Australia). This process could be applied to the Salobo deposit because magnetite grains display textures that agree with suggested features for a magmatic sulfur disproportionation in the magma sources. However, more studies are needed to get a better understanding of this process in IOCG deposits, mainly because the Salobo represent a deformed and reworked example, that affect the features of primary mineralization.

If the sulfur disproportionation process for the Salobo deposit at the magma source is feasible, the triggering agent for the sulfide precipitation would be magnetite, due to its association with chalcopyrite at early hydrothermal alteration. It has been proposed that sulfate reduction in oxidized magmas starts with ferrous iron oxidation during magnetite crystallization (i.e., process denominated as "*magnetite crisis*" by Jenner et al. 2010), accompanied by high oxygen fugacity and decreasing pH (Sun et al., 2013; Sun et al., 2015). The appearance of magnetite in the melt at ~60 wt‰ SiO_2 and Mg ~ $40_{(total\ rock)}$ decreases the $FeO_{(total)}$, switching the dissolved S from SO_4^{2-} to S^{2-}, thus generating the magmatic sulfur disproportionation (Jenner et al., 2010) (Fig. 12). Therefore, in the magmatic-hydrothermal stage (IOCG ore formation), magnetite occurs with FeO-bearing minerals (i.e., fayalite, ferrosilite, grunerite, hastingsite; Fig. 13A), which foster the oxidation (Eqs. (2) and (3)) (Sun et al., 2004; Sun et al., 2015), and thus trigger pyrite (Eq. (4)) and chalcopyrite (Eq. (5)) formation (Sun et al. 2015, and references therein) during the Cu-mineralization stage.

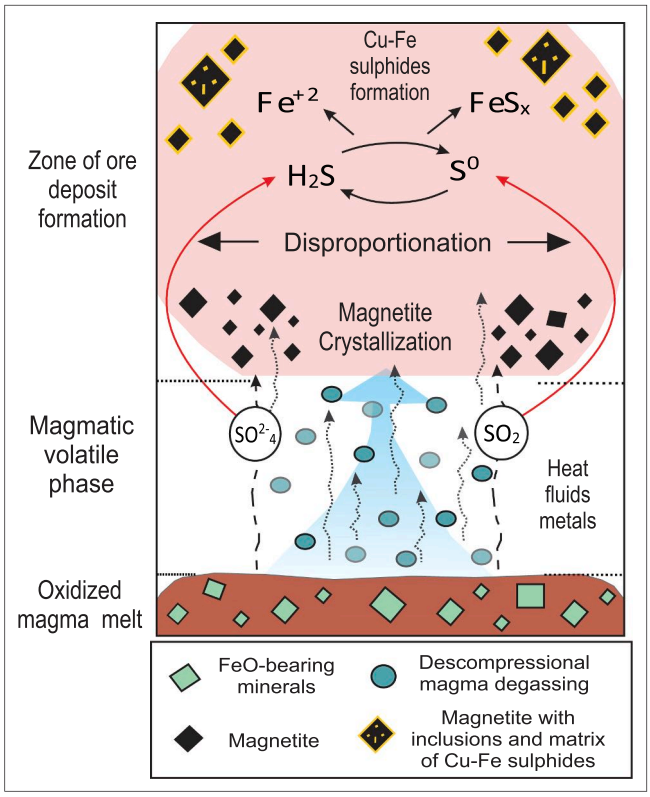

Fig. 12. Schematic diagram illustrating the role of magnetite crystallization in the sulfur disproportionation process.

$$SO_4^{2-} + 8Fe^{2+} + 8H_2O = 4Fe_2O_3 + S^{2-} + 16H^+ \quad (2)$$

$$SO_2 + 6FeO + H_2O = H_2S + 3Fe_2O_3 \quad (3)$$

$$Fe^{2+} + 2H_2S = FeS_2 + 2H^+ + H_2 \quad (4)$$

$$2Cu^+ + 2Fe^{2+} + 4H_2S = 2CuFeS_2 + 6H^+ + H_2 \quad (5)$$

Thereby, the magnetite II forming during this process coexists with sulfides and includes chalcopyrite and bornite inclusions (Figs. 12, 13A). Usually, this process is concomitant with apatite grains as inclusions in magnetite (Gelcich et al., 2005; Jenner et al., 2010). Hence, based on the isotopic data and magnetite textures (i.e., magnetite I and II), a sulfur disproportionation process is likely during the magmatic-hydrothermal stage (Cu-mineralizing phase) and, if feasible, would result in the two generations of Cu-sulfides with positive and very similar $\delta^{34}S_{V\text{-}CDT}$ values, namely, the chalcopyrite inclusions and grains and the chalcopyrite product of the pyrite replacement and matrix.

Otherwise, the similar $\delta^{34}S_{V\text{-}CDT}$ values are outstanding between bornite (de Melo et al., 2019; Santiago et al., 2021) and chalcopyrite (this study) even though these sulfides pairs are not in paragenetic equilibrium. As discussed before, chalcopyrite and bornite belong to different hydrothermal stages (i.e., Cu-mineralization and hydrolytic-propylitic, respectively). Thus, an isotopic difference would be expected instead of lower $\delta^{34}S_{V\text{-}CDT}$ values in bornite. This similarity in the isotopic signature suggests an inheritance of the sulfur isotopic signal between these two Cu-sulfides populations.

During the Paleoproterozoic granitic magmatism (Machado et al., 1991; Feio et al., 2013; Moreto et al., 2015), the fluid-rock interaction may have promoted the remobilization and reprecipitation of bornite-

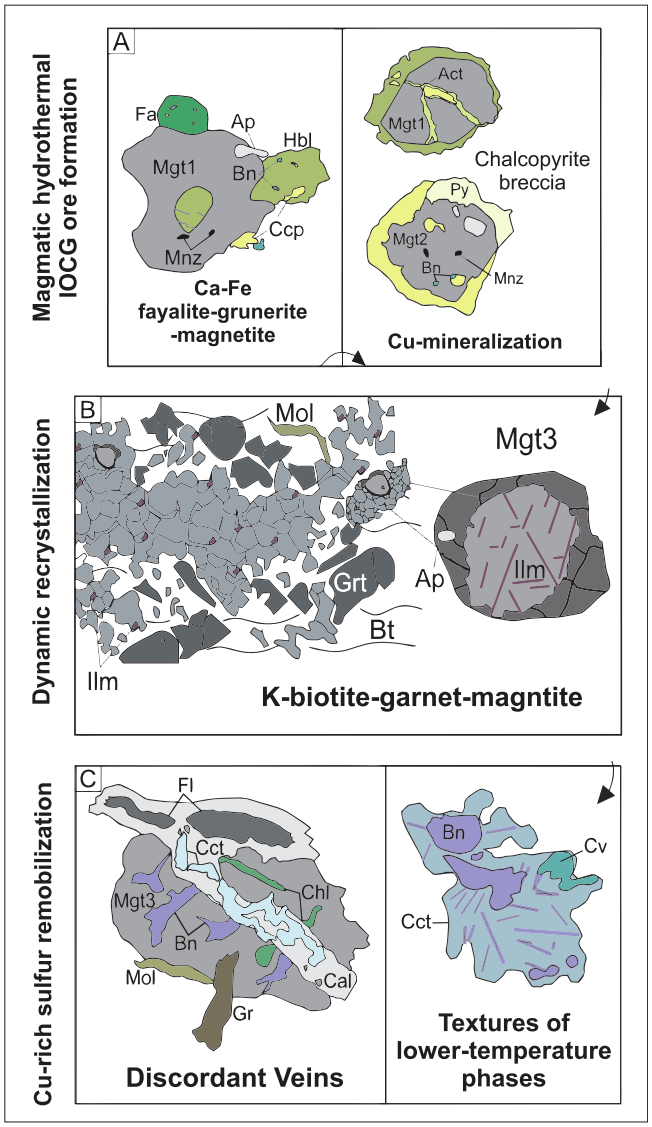

Fig. 13. Schematic diagram illustrating the three magnetite textural types and their relationship with the hydrothermal alteration evolution: (A) magmatic-hydrothermal IOCG ore formation (Mgt I and II); (B) Dynamic recrystallization (Mgt III) and (C) Cu-rich sulfur remobilization. *Abbreviations: Act: Actinolite. Ap: Apatite. Bn: Bornite. Cal: Calcite. Cct: Chalcocite. Ccp: Chalcopyrite. Chl: Chlorite. Cv: Covellite. Fa: Fayalite. Fl: Fluorite. Grt: Garnet. Gr: Graphite. Hbl: Hornblende. Ilm: Ilmenite. Mgt: Magnetite. Mnz: Monazite. Mol: Molybdenite. Py: Pyrite.*

chalcocite-digenite assemblage according to the myrmekitic-symplectititic textures (Fig. 13C), and as shown by the $\delta^{34}S_{V\text{-}CDT}$ values this process may not incorporate a new input of sulfur or had a different sulfur source. Moreover, when compared the $\delta^{34}S_{V\text{-}CDT}$ values with the isotopic ranges proposed by (Santiago et al., 2021) for the Neoarchean and Paleoproterozoic Cu-Au systems of the Carajás Domain, the results fit more with the Neoarchean intervals (-3.07 to + 3.01‰) than with those of the Paleoproterozoic (+2.17 to 4.68‰). Thus, the Neoarchean IOCG Cu-mineralization was likely the dominant magmatic sulfur source for the Salobo ore and may have obliterated any other sulfur sources. Therefore, the isotopic data suggests there was no significant new introduction of sulfur or metals in the subsequent hydrothermal events in the Salobo deposit.

On the other hand, Santiago et al. (2021) suggested that the sulfur present in sulfides from the Carajás Neoarchean and Paleoproterozoic Cu-Au systems had undergone MIF (*Mass independent fractionation*) with a dominant non-MIF-Sulfur source. MIF signature designates the fractionation effects significantly different from those expected from normal equilibrium or kinetic mass laws and processes (Johnston, 2011). The MIF of sulfur generally is recorded in a greater age than ~2400 Ma sulfates and sediments with large and variable $\delta^{34}S$, $\Delta^{33}S$, and $\Delta^{36}S$ compositions, which depend on several isotopic fractionation processes, such a gas phases reactions, the partial pressure of CO_2 (PCO_2) and hyperfine interactions in solid and liquid phases occasioned by the spin-orbit coupling effect in isotopes with odd-mass nuclei (isotopomers such as ^{33}S; Farquhar et al. 2000). However, the main source reaction that produces and preserves MIF signatures are related to atmospheric reactions (i.e., Photolysis; Farquhar et al., 2000; Johnston, 2011). In other words, the MIF signatures for the Carajás Neoarchean and Paleoproterozoic Cu-Au systems proposed by (Santiago et al., 2021) indicate that the sulfur species were in contact with the existing atmosphere and undergone photochemical reactions. The sulfur then returned to Earth's surface and participated in the ore formation.

Conversely, the Cu-Fe sulfides from the Salobo deposit, as shown by this study, render $\Delta^{33}S$ values close to zero (−0.29 to +0.09‰, Table 5) and plot (with uncertainty) within the traditional MDF-S limit (*Mass dependent fractionation – sulfur,* $\Delta^{33}S = 0 \pm 0.2$‰, Farquhar and Wing, 2003; Ohmoto et al., 2006) and close to the new proposed MDF limits by LaFlamme et al. (2018) (Fig. 9B). However, few analyses mainly of pyrrhotite are distributed outside the MDF area, which could suggest both a sulfur source with MIF processes and/or sulfur recycled from sulfur with MIF signal. Nevertheless, since the primary ore mineralization in Salobo is dominated by chalcopyrite, pyrrhotite constitutes only a minor sulfur phase and could not be considered as a reliable MIF interpretation to the sulfur source. Moreover, MDF-S processes could influence and even generate $\Delta^{33}S_{V\text{-}CDT}$ values (e.g., +0.015, Lady Bountiful, Australia; LaFlamme et al., 2018). Thus, our data reinforces that the MIF signature and the environmental-related sulfur processes that designates should be interpreted with caution.

Therefore, non-MIF processes in the sulfur source are likely for the Salobo deposit, indicating an endogenic sulfur source for the mineralizing fluid without an exogenic sulfur cycle (Rye, 1993; Halevy et al., 2010; Johnston, 2011). In this context, Bühn et al. (2012) also observed a non-MIF signature in chalcopyrite grains from the Salobo deposit. Moreover, the similar relation between the sulfur signature in bornite (hydrolytic-propylitic alteration) and chalcopyrite (Cu-mineralization), reinforces that the isotope signature was inherited, discarding a possible new input of sulfur. The MIF signature can be affected by extreme magma flux and channelized environments (LaFlamme et al., 2016) or by a new input of sulfur (Farquhar and Wing, 2003), but the similarity in the $\Delta^{33}S$ values reflects that it was not affected by dynamic geochemical processes. Besides, the small $\Delta^{33}S_{V\text{-}CDT}$ and positive $\delta^{34}S$ values denote reduced or elemental sulfur values (e.g., H_2S, HS, S_2; Farquhar et al., 2000; Farquhar and Wing, 2003) that can be generated by Mass Dependent Fractionation (MDF) (Farquhar et al., 2000; Farquhar et al., 2001; Johnston, 2011) without a sulfur source influence from evaporites or calcareous rocks with MIF record (Rye, 1993; Schlegel et al., 2017), according to the age of the host rocks in the Salobo deposit (i.e., ca. 2.70 to 2.57 Ga).

In summary, the stable isotope data support magmatic fluids' participation in the formation of the Salobo deposit, without external contribution of sulfur-rich fluids during the hydrothermal evolution.

5.3. *Timing of IOCG mineralization: implication for the formation and remobilization of the Salobo IOCG deposit*

The geological and metallogenetic history of the Salobo deposit involves multiple superimposed hydrothermal alteration events, metamorphism along a major transcurrent shear zone, and granitic intrusions (de Melo et al., 2019). During the Neoarchean volcanism, a high-temperature magmatic-hydrothermal magnetite-forming fluid shaped the first pre-ore stage characterized by Na-scapolite and Ca-Fe (fayalite-

grunerite-magnetite I) alterations (Fig. 13A).

According to the association of magnetite I with high-temperature minerals (i.e., fayalite and ferrosilite; Fig. 13A), the $\delta^{34}S$ values (Fig. 9) and the magnetite chemical signature; the crystallization of magnetite during the magma differentiation could lead to ferrous Fe oxidation, and thus to magmatic sulfur disproportionation. Thereby, magnetite precipitation triggered the sulfate reduction (Fig. 12), promoting the formation of Cu-Fe sulfides (i.e., chalcopyrite and pyrite; Fig. 13) in the later or at least outlasting Cu-mineralization stage – magnetite II (Fig. 13A). Besides, one fraction of the chalcopyrite precipitation occurred due to a Cu-bearing fluid reaction with a Fe^{2+}-bearing reductant (i.e., pyrite replacement).

The sulfur signature (Fig. 9) and ore textures similar to those that occurs in high-temperature and low-pressures oxidized-hydrothermal systems (Rye, 1993; Sun et al., 2015; Schlegel et al., 2017), suggest that minimal or no external sulfur was present in the mineralizing source, in agreement with negligible mass-independent fractionation and narrower $\delta^{34}S$ results (Fig. 9; Rye, 1993). Thus, the two generations of Cu-rich sulfides resulted in chalcopyrite-rich breccias at the Cu-mineralizing stage, indicating that the highly oxidized fluid may have been enough to contribute to the bulk Cu grade in Salobo.

Following, the influence of granitic magmatism and later medium-to-low grade metamorphic events at ca. ~2.55 Ga, associated with the tectonic reactivation of the Cinzento Shear Zone, probably induced the remobilization and recrystallization of previous Fe-Cu-rich stages, resulting in the granoblastic magnetite III assemblages (Fig. 13B), which inherited the trace element signatures of magnetite I and II. Finally, we suggest that the Paleoproterozoic alkaline to sub–alkaline A-type magmatism (Machado et al., 1991; Lindenmayer and Teixeira, 1999; Pollard et al., 2018) promoted ore-sulfur remobilization of the previous Cu-rich sulfides (Cu mineralization assemblage), resulting in discordant brittle veins of bornite, digenite, chalcocite, and covellite associated with fluorite and calcite in the magnetite-rich schists (Fig. 13C). This remobilization did not produce a new magnetite population. Conversely, it is just characterized by the Cu-sulfur reconcentration (Valadão, 2019).

In summary, the Salobo "high-grade ore" represents mainly a Neoarchean IOCG Cu-mineralization ore that underwent later hydrothermal events (ca. 2.5 Ga and Paleoproterozoic) which resulted in the bornite-chalcocite-digenite assemblage in the magnetite schist.

6. Conclusions

This study provided new insights into the metamorphosed Salobo IOCG deposit through a comprehensive analysis of the mineralogical and isotopic data:

- The mineralogical association found (i.e., magnetite-chalcopyrite) suggests that the main metallogenetic event in the Salobo deposit must be related to Neoarchean magmatism as well as other IOCG deposits in Carajás Mineral Province.
- The sulfur isotopic composition indicates the primary sulfur source as magmatic with insights into the sulfur disproportionation process related to magnetite precipitation.
- Early stages of hydrothermal alteration are represented by Mgt I and II, which underwent CDR (couple-dissolution-reprecipitation) processes resulting in Mgt III. Despite the post-formation processes related to the dynamic metamorphism, the magnetite types share a similar chemical composition that suggests the same magmatic-hydrothermal origin for all of them.
- The Salobo deposit may represent a metamorphosed IOCG Cu-mineralization, in which subsequent fluid-rock processes were responsible for the Cu-enrichment in a distinctive assemblage of bornite-digenite-chalcocite hosted by magnetite-rich rocks.

Declaration of Competing Interest

The authors declare that they have no known competing financial interests or personal relationships that could have appeared to influence the work reported in this paper.

Acknowledgements

Dr Heejin Jong is especially appreciated for the analytical support. We also would like to thank the VALE for providing access to the company's data and for supporting field activities, as well as to the Instituto de Geociências of the University of Brasília for the analytical facilities. YTCR, MES, and CG acknowledge the CNPq and the Swedish Research Council Link Programme for continuous funding through research grants. This study is part of the first author's (Yuri Tatiana Campo Rodríguez) M.Sc. dissertation developed at the University of Brasília, which was financed in part by the Coordenação de Aperfeiçoamento de Pessoal de Nível Superior – Brasil (CAPES) – Finance Code 001.

Appendix A. Supplementary data

Supplementary data to this article can be found online at https://doi.org/10.1016/j.oregeorev.2021.104572.

References

Acosta-Góngora, P., Gleeson, S.A., Samson, I.M., Ootes, L., Corriveau, L., et al., 2014. Trace element geochemistry of magnetite and its relationship to Cu-Bi-Co-Au-Ag-U-W mineralization in the great bear magmatic zone, NWT, Canada. Economic Geology 109 (7), 1901–1928. https://doi.org/10.2113/econgeo.109.7.1901.

Araújo Filho, R.C., Nogueira, A.C.R., Araújo, R.N., 2020. New stratigraphic proposal of a Paleoproterozoic siliciclastic succession: Implications for the evolution of the Carajás Basin, Amazonian craton, Brazil. J. S. Am. Earth Sci. 102, 102665. https://doi.org/10.1016/j.jsames.2020.102665.

Avelar, V.G., Lafon, J.M., Correia Jr., F.C., Macambira, E.M.B., 1999. O magmatismo arqueano da região de Tucumã - Província Mineral De Carajás: Novos resultados geocronológicos. Revista Brasileira de Geociências 29, 453–460.

Barton, MD, University of Arizona, 2014. Iron Oxide(-Cu-Au-REE-P-Ag-U-Co) Systems. Treatise on Geochemistry: Second Edition, , 2nd13. Elsevier Ltd, pp. 515–541.

Bernard Prado, E., Tavares, F., Sicoli Seoane, J. C., Ganade, C., Cezar mendes, J., and Kyley Oliveira, J., 2019, Tectonic setting and structural controls of the giant Salobo modified IOCG deposit, Carajás Mineral Province, Brazil: evidences from multi-scale structural analysis and mineral chemistry: Ore Geology Reviews.

Bühn, B., Santos, R.V., Dardenne, M.A., de Oliveira, C.G., 2012. Mass-dependent and mass-independent sulfur isotope fractionation (δ34S and δ33S) from Brazilian Archean and Proterozoic sulfide deposits by laser ablation multi-collector ICP-MS. Chem. Geol. 312-313, 163–176.

Canil, D., Lacourse, T., 2020. Geothermometry using minor and trace elements in igneous and hydrothermal magnetite. Chem. Geol. 541, 119576. https://doi.org/10.1016/j.chemgeo.2020.119576.

Corriveau, L., Montreuil, J.-F., Potter, E.G., 2016. Alteration facies linkages among iron oxide copper-gold, iron oxide-apatite, and affiliated deposits in the great bear magmatic zone, Northwest Territories, Canada. Econ. Geol. 111 (8), 2045–2072.

da Costa, F.G., Araújo dos Santos, P., de Oliveira, C., Serafim, I.C., Lima Costa, I.S., Roopnarain, S., 2020. From Mesoarchean drips to modern–style tectonics in the Carajás Province, Amazonian Craton. J. S. Am. Earth Sci. 104.

Dall'Agnol, R., Oliveira, M.A., Almeida, J.A.C., Althoff, F.J., Leite, A.A.S., Oliveira, D.C., Barros, C.E.M., 2006. Archean and Paleoproterozoic granitoids of the Carajás Metallogenic Province, eastern Amazonian craton. In: Symposium on Magmatism, Crustal Evolution, and Metallogenesis of the Amazonian Craton; Abstracts Volume and Field Trips Guide, p. 150.

Dare, S.A.S., Barnes, S.-J., Beaudoin, G., Méric, J., Boutroy, E., Potvin-Doucet, C., 2014. Trace elements in magnetite as petrogenetic indicators. Miner. Deposita 49 (7), 785–796.

Deditius, A.P., Reich, M., Simon, A.C., Suvorova, A., Knipping, J., Roberts, M.P., Rubanov, S., Dodd, A., Saunders, M., 2018. Nanogeochemistry of hydrothermal magnetite. Contrib. Miner. Petrol. 173, 1–20.

Delinardo da Silva, M. A., 2014,Metatexitos e Diatexitos do Complexo Xingu na região de Canaã dos Carajás: Implicações para a evolução mesoarqueana do domínio Carajás: Universidade Estadual de Campinas, Brazil: 102 p.

DOCEGEO, 1988. Revisão litoestratigráfica da Província Mineral de Carajás - Litoestratigrafia e principais depósitos minerais. Congresso Brasileiro de Geologia 35th, 11–54.

Droop, G.T.R., 1987. A general equation for estimating Fe 3+ concentrations in ferromagnesian silicates and oxides from microprobe analyses, using stoichiometric criteria. Mineral. Mag. 51 (361), 431–435.

Dupuis, Céline, Beaudoin, G., 2011. Discriminant diagrams for iron oxide trace element fingerprinting of mineral deposit types. Miner. Deposita 46 (4), 319–335.

Farquhar, J., Wing, B.A., 2003. Multiple sulfur isotopes and the evolution of the atmosphere. Earth Planet. Sci. Lett. 213 (1-2), 1–13.
Farquhar, J., Bao, H., Thiemens, M., 2000. Atmospheric influence of Earth's earliest sulfur cycle. Science 289 (5480), 756–758.
Farquhar, J., Savarino, J., Airieau, S., Thiemens, M.H., 2001. Observation of wavelength-sensitive mass-independent sulfur isotope effects during SO2 photolysis: Implications for the early atmosphere. J. Geophys. Res. 106 (E12), 32829–32839.
Feio, G.R.L., Dall'Agnol, R., Dantas, E.L., Macambira, M.J.B., Santos, J.O.S., Althoff, F.J., Soares, J.E.B., 2013. Archean granitoid magmatism in the Canaã dos Carajás area: Implications for crustal evolution of the Carajás province, Amazonian craton, Brazil. Precambr. Res. 227, 157–185.
Ferreira Filho, C. F., Cançado, F., Correa, C., Macambira, E. M. B., Siepierski, L., and Brod, T. C. J., 2007, Mineralizações estratiformes de EGP-Ni associadas a complexos acamadados em Carajás: os exemplos de Luanga e Serra da Onça, in Contribuições à Geologia da Amazônia.: Belém - Pará, p. Sociedade Brasileira de Geología-Núcleo Norte.
Gelcich, S., Davis, D.W., Spooner, E.T.C., 2005. Testing the apatite-magnetite geochronometer: U-Pb and 40Ar/ 39Ar geochronology of plutonic rocks, massive magnetite-apatite tabular bodies, and IOCG mineralization in Northern Chile. Geochim. Cosmochim. Acta 69 (13), 3367–3384.
Grainger, C.J., Groves, D.I., Tallarico, F.H.B., Fletcher, I.R., 2008. Metallogenesis of the Carajás Mineral Province, Southern Amazon Craton, Brazil: Varying styles of Archean through Paleoproterozoic to Neoproterozoic base- and precious-metal mineralisation. Ore Geol. Rev. 33 (3-4), 451–489.
Halevy, I., Johnston, D. T., and Schrag, D. P., 2010, Explaining the Structure of the Archean Mass-Independent Sulfur Isotope Record:, accessed at Science.
Harlov, D.E., Wirth, R., Hetherington, C.J., 2011. Fluid-mediated partial alteration in monazite: The role of coupled dissolution-reprecipitation in element redistribution and mass transfer. Contrib. Miner. Petrol. 162 (2), 329–348.
Hitzman, Murray W., Naomi, Oreskes, Einaudi, Marco T., et al., 1992. Geological characteristics and tectonic setting of proterozoic iron oxide (CuUAuREE) deposits. Precambrian Research 58 (1–4), 241–287. https://doi.org/10.1016/0301-9268(92)90121-4.
Hu, H., Li, J.-W., Lentz, D., Ren, Z., Zhao, X.-F., Deng, X.-D., Hall, D., 2014. Dissolution-reprecipitation process of magnetite from the Chengchao iron deposit: Insights into ore genesis and implication for in-situ chemical analysis of magnetite. Ore Geol. Rev. 57, 393–405.
Hu, H., Lentz, D., Li, J.-W., McCarron, T., Zhao, X.-F., Hall, D., 2015. Reequilibration processes in magnetite from iron skarn deposits. Econ. Geol. 110 (1), 1–8.
Huang, X. W., and Beaudoin, G., 2019, Textures and chemical compositions of magnetite from iron oxide copper-gold (IOCG) and kiruna-type iron oxide-apatite (IOA) deposits and their implications for ore genesis and magnetite classification schemes: Economic Geology, v. 114, p. 953–979.
Huhn Bacelar, S.R., 1996. São os depósitos cupríferos de Carajás do tipo Cu-Au-U-(ETR)?. In: Sociedade Brasileira de Geologia, N, N. ed. Boletim de Resumos Expandidos e Guia de Excursões, Belém - Pará, pp. 140–143.
Jenner, F. E., O'Neill, H. S. C., Arculus, R. J., and Mavrogenes, J. A., 2010, The magnetite crisis in the evolution of arc-related magmas and the initial concentration of Au, Ag and Cu: Journal of Petrology, v. 51, p. 2445–2464.
Johnston, D.T., 2011. Multiple sulfur isotopes and the evolution of Earth's surface sulfur cycle. Earth Sci. Rev. 106 (1-2), 161–183.
Justo, A.P., Dantas, E.L., Bau, M., Freitas-Silva, F.H., Santos, R.V., Schorscher, J.H.D., 2020. Paleobasinal to band-scale REE + Y distribution in iron formations from Carajás, Amazon Craton, Brazil. Ore Geol. Rev. 127, 103750.
Knipping, J.L., Bilenker, L.D., Simon, A.C., Reich, M., Barra, F., Deditius, A.P., Wälle, M., Heinrich, C.A., Holtz, F., Munizaga, R., 2015. Trace elements in magnetite from massive iron oxide-apatite deposits indicate a combined formation by igneous and magmatic-hydrothermal processes. Geochim. Cosmochim. Acta 171, 15–38.
LaFlamme, C., Martin, L., Jeon, H., Reddy, S.M., Selvaraja, V., Caruso, S., Bui, T.H., Roberts, M.P., Voute, F., Hagemann, S., Wacey, D., Littman, S., Wing, B., Fiorentini, M., Kilburn, M.R., 2016. In situ multiple sulfur isotope analysis by SIMS of pyrite, chalcopyrite, pyrrhotite, and pentlandite to refine magmatic ore genetic models. Chem. Geol. 444, 1–15.
LaFlamme, C., Jamieson, J.W., Fiorentini, M.L., Thébaud, N., Caruso, S., Selvaraja, V., 2018. Investigating sulfur pathways through the lithosphere by tracing mass independent fractionation of sulfur to the Lady Bountiful orogenic gold deposit. Yilgarn Craton: Gondwana Research 58, 27–38.
Lindenmayer, Z. G., 1990,Salobo sequence, Carajás, Brasil: Geology, geochemistry and metamorphism: Western University: 407 p.
Lindenmayer, Z.G., Teixeira, J.B.G., 1999. Ore genesis at the Solobo copper deposit. Base Metal Deposits of Brazil, Serra dos Carajás, pp. 33–43.
Machado, N., Lindenmayer, Z., Krogh, T.E., Lindenmayer, D., 1991. U-Pb geochronology of Archean magmatism and basement reactivation in the Carajás area, Amazon shield, Brazil. Precambr. Res. 49 (3-4), 329–354.
Mansur, E.T., Ferreira Filho, C.F., Oliveira, D.P.L., 2020. The Luanga deposit, Carajás Mineral Province, Brazil: Different styles of PGE mineralization hosted in a medium-size layered intrusion. Ore Geol. Rev. 118, 103340. https://doi.org/10.1016/j.oregeorev.2020.103340.
Martins, P.L.G., Toledo, C.L.B., Silva, A.M., Chemale Jr, F., Santos, João.O.S., Assis, L.M., 2017. Neoarchean magmatism in the southeastern Amazonian Craton, Brazil: Petrography, geochemistry and tectonic significance of basalts from the Carajás Basin. Precambr. Res. 302, 340–357.
Melo, G., Monteiro, L. V. S., Xavier, R. P., Moreto, C. P. N., Santiago, E. S. B., Dufrane, S. A., Aires, B., and Santos, A. F. F., 2017, Temporal evolution of the giant Salobo IOCG deposit, Carajás Province (Brazil): constraints from paragenesis of hydrothermal alteration and U-Pb geochronology: Mineralium Deposita, v. 52, p. 709–732.
Melo, G. H. C. de, Monteiro, L. V. S., Xavier, R. P., Moreto, C. P. N., and Santiago, E., 2019, Tracing fluid sources for the salobo and Igarapé Bahia deposits: Implications for the genesis of the iron oxide copper-gold deposits in the Carajás Province, Brazil: Economic Geology, v. 114, p. 697–718.
Montreuil, J.-F., Potter, E.G., Corriveau, L., Davis, W.J., 2016. Element mobility patterns in magnetite-group IOCG systems: The Fab IOCG system, Northwest Territories, Canada. Ore Geol. Rev. 72, 562–584.
Moreto, C. P. N., Monteiro, L. V. S., Xavier, R. P., Creaser, R. A., DuFrane, S. A., Tassinari, C. C. G., Sato, K., Kemp, A. I. S., and Amaral, W. S., 2015, Neoarchean and paleoproterozoic iron oxide-copper-gold events at the sossego deposit, Carajás Province, Brazil: Re-Os and U-Pb geochronological evidence: Economic Geology, v. 110.
Nadoll, P., Angerer, T., Mauk, J.L., French, D., Walshe, J., 2014. The chemistry of hydrothermal magnetite: A review. Ore Geol. Rev. 61, 1–32.
Nadoll, P., Mauk, J.L., Leveille, R.A., Koenig, A.E., 2015. Geochemistry of magnetite from porphyry Cu and skarn deposits in the southwestern United States. Miner. Deposita 50 (4), 493–515.
Nogueira, A. C. R., Truckenbrodt, W., and Pinheiro, R. V. L., 1995, Formação Águas Claras, Pré-Cambriano da Serra dos Carajás: redescrição e redefinição litoestratigráfica: Boletim do Museu Paraense Emílio Goeldi, v. 7, p. 177–277.
Ohmoto, H., Watanabe, Y., Ikemi, H., Poulson, S.R., Taylor, B.E., 2006. Sulphur isotope evidence for an oxic Archaean atmosphere. Nature 442 (7105), 908–911.
Pidgeon, R.T., Macambira, M.J.B., Lafon, J.M., 2000. Th-U-Pb isotopic systems and internal structures of complex zircons from an enderbite from the Pium Complex, Carajas Province, Brazil: Evidence for the ages of granulite facies metamorphism and the protolith of the enderbite. Chem. Geol. 166, 159–171.
Pinheiro, R.V.L., Holdsworth, R.E., 2000. Eevolução tectonoestratigráfica dos sistemas transcorrentes Carajás e cinzento, Cinturão Itacaiúnas, na borda leste do Craton Amazónico, Pará. Revista Brasileira de Geociências 30, 597–606.
Pollard, P.J., 2006. An intrusion-related origin for Cu-Au mineralization in iron oxide-copper-gold (IOCG) provinces. Mineralium Deposita 41 (2), 179–187. https://doi.org/10.1007/s00126-006-0054-x.
Pollard, P. J., Taylor, R. G., Peters, L., Matos, F., Freitas, C., Saboia, L., and Huhn, S., 2018, Ar- 39 Ar dating of Archean iron oxide Cu-Au and Paleoproterozoic granite-related Cu-Au deposits in the Carajás Mineral Province , Brazil : implications for genetic models: Mineralium Deposita.
Requia, K., and Fontboté, L., 1999, Hydrothermal alkali metasomatism in the Salobo iron oxide Cu (-Au) deposit, Carajás Mineral Province, northern Brazil: Mineral deposits, p. 1025–1028.
Requia, K., and Fontboté, L., 2000, The Salobo Iron Oxide Copper-Gold Deposit, Carajás, Northern Brazil: Porter, TM, Hydrothermal Iron Oxide Copper-Gold & Related Deposits: A Global Perspective, v. 1, p. 225–236.
Requia, K., Stein, H., Fontboté, L., Chiaradia, M., 2003. Re-Os and Pb-Pb geochronology of the Archean Salobo iron oxide copper-gold deposit, Carajás mineral province, northern Brazil. Mineralium Deposita 38, 727–738.
Richards, Jeremy P., Mumin, A. Hamid, 2013. Magmatic-hydrothermal processes within an evolving Earth: Iron oxide-copper-gold and porphyry Cu ± Mo ± Au deposits. Geology 41 (7), 767–770. https://doi.org/10.1130/G34275.1.
Rojas, P.A., Barra, F., Deditius, A., Reich, M., Simon, A., Roberts, M., Rojo, M., 2018. New contributions to the understanding of Kiruna-type iron oxide-apatite deposits revealed by magnetite ore and gangue mineral geochemistry at the El Romeral deposit, Chile. Ore Geol. Rev. 93, 413–435.
Ruiz-Agudo, E., Putnis, C.V., Putnis, A., 2014. Coupled dissolution and precipitation at mineral-fluid interfaces. Chem. Geol. 383, 132–146.
Rye, R. O., 1993. The Evolution of Magmatic Fluids in the Epithermal Environment: The Stable Isotope Perspective: Economic Geology, v. 88, p. 733–753.
Santiago, E.S.B., Xavier, R.P., Hagemann, S.G., Monteiro, L.V.S., Cliff, J., 2021. Multiple sulfur isotopes constraints on origin and evolution of the Neoarchean and Paleoproterozoic Cu-Au systems from the Carajás Domain, Amazonian Craton, Brazil. Ore Geol. Rev. 129, 103872. https://doi.org/10.1016/j.oregeorev.2020.103872.
Schlegel, T.U., Wagner, T., Boyce, A., Heinrich, C.A., 2017. A magmatic source of hydrothermal sulfur for the Prominent Hill deposit and associated prospects in the Olympic iron oxide copper-gold (IOCG) province of South Australia. Ore Geol. Rev. 89, 1058–1090.
Siepierski, L., Ferreira Filho, C.F., 2016. Spinifex-textured komatiites in the south border of the Carajas ridge, Selva Greenstone belt, Carajás Province, Brazil. J. S. Am. Earth Sci. 66, 41–55.
Silva, R.C.F., Hagemann, S., Lobato, L.M., Rosière, C.A., Banks, D.A., Davidson, G.J., Vennemann, T., Hergt, J., 2013. Hydrothermal fluid processes and evolution of the giant serra norte jaspilite-hosted iron ore deposits, carajás mineral Province, Brazil. Econ. Geol. 108, 739–779.
Souza, L. H., and Vieira, E. A. P., 2000, Salobo 3 Alpha Deposit: Geology and Mineralisation, in Porter T M ed., Hydrothermal Iron Oxide Copper-Gold & Related Deposits: A Global Perspective,: PGC Publishing, p. 213–224.
Souza, S. Z., Dall'Agnol, R., Althoff, F. J., Leite, A. A. S., and Barros, C. E. M., 1996, Carajás mineral province: geological, geochronological and tectonic constrasts on the Archean evolution of the Rio Maria Granite-Greenstone Terrain and the Carajás block., in Symposium on Archean Terranes of South America Platform, Brasília:, p. Extended abstracts. SBG, pp 31-32.
Sun, W., Arculus, R.J., Kamenetsky, V.S., Binns, R.A., 2004. Release of gold-bearing fluids in convergent margin magmas prompted by magnetite crystallization. Nature 431 (7011), 975–978.
Sun, W., Huang, R.-fang., Li, H., Hu, Y.-bin., Zhang, C.-chan., Sun, S.-jun., Zhang, L.-peng., Ding, X., Li, C.-ying., Zartman, R.E., Ling, M.-xing., 2015. Porphyry deposits and oxidized magmas. Ore Geol. Rev. 65, 97–131.

Sun, W.-dong., Liang, H.-ying., Ling, M.-xing., Zhan, M.-zhen., Ding, X., Zhang, H., Yang, X.-yong., Li, Y.-liang., Ireland, T.R., Wei, Q.-rong., Fan, W.-ming., 2013. The link between reduced porphyry copper deposits and oxidized magmas. Geochim. Cosmochim. Acta 103, 263–275.

Tassinari, C.C.G., Mellito, Kátia.M., Babinski, M., 2003. Age and origin of the Cu (Au-Mo-Ag) Salobo 3A ore deposit, Carajas Mineral Province, Amazonian Craton, northern Brazil. Episodes 26 (1), 2–9.

Tavares, F.M., Trouw, R.A.J., da Silva, Cíntia.M.G., Justo, A.P., Oliveira, J.K.M., 2018. The multistage tectonic evolution of the northeastern Carajás Province, Amazonian Craton, Brazil: Revealing complex structural patterns. J. S. Am. Earth Sci. 88, 238–252.

Toledo, P. I. de F., Moreto, C. P. N., Xavier, R. P., Gao, J., de Matos, J. H. da S. N., and de Melo, G. H. C., 2018, Multistage evolution of the Neoarchean (ca. 2.7 Ga) Igarapé cinzento (GT-46) iron oxide copper-gold deposit, Cinzento shear zone, Carajás Province, Brazil: Economic Geology, v. 114, p. 1–34.

Urai, J. L., Means, W. D., and Lister, G. S., 1986. Dynamic recrystallization of minerals (B. E. Honns & H. C. Heard, Eds.): Mineral and rock deformation: Laboratory studies: American Geophysical Union, Geophysical Monograph, 161–199 p.

Valadão, L.V., 2019. A review of the hydrothermal alteration stages in the giant metamorphosed IOCG Salobo deposit, Carajás Mineral Province. Unpublished MSc. dissertation:. Universidade de Brasília, Brazil, p. 76 p..

VALE, 2012, Vale obtains operation license for Salobo. (http://saladeimprensa.vale.com/Paginas/ImprensaDetalhe.aspx?t=Online&iID=675).

Vasquez, M. L., Da Rosa-Costa, L. T., Silva, C., Ricci, P., Barbosa, J., Klein, E., Lopes, E., Macambira, E., Chaves, C., Carvalho, J., Oliveira, J., Anjos, G., and Silva, H., 2008, Geologia e Recursos Minerais do Estado do Pará: Sistema de Informações Geográficas - SIG: texto explicativo dos mapas Geológico e Tectônico e de Recursos Minerais do Estado do Pará. Organizadores, Marcelo Lacerda Vasquez, Lúcia Travassos da Rosa-Costa.: CPRM, Belém.

Wang, R. C., Yu, A. P., Chen, J., Xie, L., Lu, J. J., and Zhu, J. C., 2012, Cassiterite exsolution with ilmenite lamellae in magnetite from the Huashan metaluminous tin granite in southern China: Mineralogy and Petrology, v. 105, p. 71–84.

Wen, G., Li, J., Hofstra, A.H., Koenig, A.E., Lowers, H.A., Adams, D., 2017. Hydrothermal reequilibration of igneous magnetite in altered granitic plutons and its implications for magnetite classification schemes : Insights from the Handan-Xingtai iron district, North China Craton. Geochimica et Cosmochimica Acta 213, 255–270.

Whitehouse, M.J., 2013. Multiple Sulfur Isotope Determination by SIMS: Evaluation of Reference Sulfides for Δ33S with Observations and a Case Study on the Determination of Δ36S. Geostand. Geoanal. Res. 37, 19–33.

Whitehouse, M.J., Kamber, B.S., Fedo, C.M., Lepland, A., 2005. Integrated Pb- and S-isotope investigation of sulphide minerals from the early Archaean of southwest Greenland. Chem. Geol. 222 (1-2), 112–131.

Williams, Patrick J., Barton, Mark D., Johnson, David A., Fontboté, Lluís, de Haller, Antoine, Mark, Geordie, Oliver, Nicholas H.S., Marschik, Robert, et al., 2005. Iron oxide copper-gold deposits: Geology, space-time distribution, and possible modes of origin. Economic Geology 100th Anniversary, 371–405. https://doi.org/10.5382/AV100.13.